SPECTROSCOPIC ANALYSIS OF A MAGNETOPLASMA DYNAMIC ARCJET

by

Daniel B. Kilfoyle

S.B. Aeronautics and Astronautics
Massachusetts Institute of Technology (1986)

SUBMITTED IN PARTIAL FULFILLMENT
OF THE REQUIREMENTS OF THE
DEGREE OF

MASTER OF SCIENCE

in

AERONAUTICS AND ASTRONAUTICS

at the

MASSACHUSETTS INSTITUTE OF TECHNOLOGY

January 1988

Signature of Author_____
Department of Aeronautics and Astronautics
January 15, 1988

Certified by_____
Professor Manuel Martinez-Sanchez
Thesis Supervisor

Accepted by_____
Professor Harold Y. Wachman
Chairman, Departmental Graduate Committee

SPECTROSCOPIC ANALYSIS OF A MAGNETOPLASMA DYNAMIC ARCJET

by

DANIEL B. KILFOYLE

Submitted to the Department of Aeronautics and Astronautics
on January 15, 1988, in partial fulfillment of the
requirements for the Degree of Master of Science in
Aeronautics and Astronautics

ABSTRACT

A spectroscopic data acquisition system was developed for plasma discharges. The system can rapidly determine plasma properties such as temperature and density with temporal resolution as high as 100 nanoseconds and spatial resolution as low as 0.5 millimeters. System response and linearity was documented and overall performance was investigated using a magnetoplasma dynamic (MPD) discharge of argon.

An efficient and flexible signal processing methodology was developed. Two important processing features were an Abel inversion based on the fast Fourier transform and a well defined noise filtering procedure.

Electron temperature was found to be reduced by nearly 35% (from a little more than two to about one and a half electron volts) when a constant radius cathode was replaced by a flared cathode. Furthermore, electron temperature behavior during the initial transient and during the severe voltage fluctuations commonly called onset was studied. Temperatures were principally determined using the relative line intensity method.

Electron density was measured with Stark broadening theory. Hydrogen ionization fractions near unity severely limited the success of this measurement but density estimates were nevertheless possible. Electron density approximately varies from 10^{15} cm^{-3} near the cathode to 10^{14} cm^{-3} near the anode.

Preliminary indications of ion temperature were found suggesting the existence of ion to electron temperature ratios greater than one. A possible explanation for this behavior is given.

The acquisition system was deemed successful and future studies are suggested.

Thesis Supervisor: Dr. Manuel Martinez–Sanchez

Title: Associate Professor of Aeronautics and Astronautics

ACKNOWLEDGEMENT

I would like to offer sincere thanks to my advisor, Dr. Manuel Martinez–Sanchez for offering me this splendid opportunity to learn. Beyond that, his guidance and ideas for overcoming theoretical and experimental obstacles were invaluable.

I want my two coworkers, Daniel Heimerdinger and John Davis, to know that their constant help and simple companionship made this experiment a pleasurable and successful experience.

I would also to like to extend a special thanks to Kevin Rhoads. Without his help, this may not have been possible. In addition, I appreciate the support that the U.S. Air Force Office of Scientific Research has given this project (AFOSR–86–0119).

Finally, I want to thank my wife and friend, Heidi, for everything.

TABLE OF CONTENTS

LIST OF FIGURES

LIST OF SYMBOLS

		Page
A	Advection rate [sec^{-1}]	31
A_{mn}	Transition probability from state n to m [sec^{-1}]	26
B	Bandwidth of noise	23
C_n	Collisional transition rate [sec^{-1}]	30
D	Ambipolar diffusion rate [sec^{-1}]	30
d_p	Pinhole radius [m]	44
E_m	Excitation energy of state m [eV]	26
f	Oscillator strength [m^2/sec]	26
f_l	Focal length of lens [m]	44
f_n	Frequency of noise	23
Δf	Percent uncertainty in oscillator strength	27
FT[]	Fourier transform operator	21
g_m	Degeneracy of state m	26
G_n	Spectral power density	23
I	Intensity [W/m^2/steradian]	20
ΔI	Percent uncertainty in intensity	27
J_o	Zero order Bessel function	21
L	Characteristic length [m]	30
l_{lp}	Pinhole lens separation [m]	44
M	Mach number	67
$\dot{m}$	Mass flow [kg/sec]	65
M_a	Atomic mass [kg]	65
N	Total number density of species [m^{-3}]	26
n	Principal quantum number	30

n_e	Electron density [cm^{-3}]	29
N_i	Number density in state i [m^{-3}]	26
Q	Partition function	26
R	Radius [m]	20
r	Radial coordinate	20
R_n	Radiative transition rate [sec^{-1}]	30
R_3	Three–body recombination rate [sec^{-1}]	30
T	Particle temperature [K]	33
T_{ia}	Ion temperature after shock [K]	67
T_{ib}	Ion temperature before shock [K]	67
T_e	Electron temperature [eV]	26
ΔT_e	Percent uncertainty in electron temperature	27
V	Characteristic velocity [m/sec]	31
V_{avg}	Average velocity [m/sec]	65
X_h	Ionization potential of hydrogen [eV]	30
X_i	Ionization potential [eV]	29
X_t	Thermal limit [eV]	29
y	Vertical coordinate	20
z	Number of effective charges in nucleus	29
α	Ionization fraction, n_e/n_t	61
δd	Spatial resolution [m]	44
ϵ	Emission coefficient [W/m^3/steradian]	20
ϵ_f	Ratio of densities across shock	67
γ	Ratio of specific heats	67
λ	Wavelength [Å]	33
λ_d	Doppler full width at half maximum [Å]	64

λ_l	Lorentzian full width at half maximum [Å]	64
λ_t	Total full width at half maximum [Å]	64
Λ	Tabulated function of T_e	30
μ	Atomic weight [atomic units]	33
ϕ_c	Cone angle [degrees]	67
ϕ_s	Shock angle [degrees]	67
σ	Standard deviation	28

CHAPTER 1

Introduction

Magnetoplasma dynamic (MPD) thrusters are a class of electric propulsion devices which show particular promise for future space missions. MPD thrusters have demonstrated the high specific impulses characteristic of electric propulsion devices, between 800 and 3000 seconds, while providing a relatively high level of thrust. For these reasons, MPD's have been the subject of numerous investigations over the past two decades. While experimental efforts to improve performance have been the norm, significant advances are being made by theoretical investigations such as those by Professor Martinez–Sanchez[1,2] of the Massachusetts Instiute of Technology, Dr. Kuriki of the Japan Institute of Space and Astronautical Science[3,4], and Dr. King[5] of the Jet Propulsion Laboratory. In order to test the validity of these models and to guide their future development, accurate measurements of plasma parameters such as electron temperature, electron density, and heavy particle temperature are crucial. As many of these devices operate in pulsed mode, attention must also be given to time resolved measurements. The purpose of this study is to develop a single non–intrusive diagnostic apparatus capable of measuring these plasma parameters rapidly, accurately, and with both temporal and spatial resolution. The requirement of non–intrusiveness essentially limits the system to optical techniques. Probe techniques have the decided disadvantage of disturbing the plasma by generating shocks, stagnation points, and impurities. In the presence of substantial transverse and axial gradients, spatial resolution is critical. Unfortunately, to obtain spatial resolution, one must acquire a great deal of data. The shear volume of data necessary demands rapid data acquisition. Finally, pulsed plasmas can have significant start–up transients. Time resolution is essential to seperate the transient behavior from the steady state behavior as well as to enable study of the transient conditions themselves. The following sections will explore the available optical techniques.

Typical values of MPD plasma properties should be kept in mind when reviewing the following diagnostic techniques. Electron densities are generally 10^{15} electrons per cm^{-3}. In general, this value can be higher or lower by an order of magnitude depending on the specific device. Electron temperatures approximately range between 10000 and 20000 Kelvin. The ion temperature range in these devices is not well defined but conventional thought holds it to somewhat lower than the electron temperature. There are, however, some indications that it may be as much as five times higher than the electron temperature.

1.1 Density measurements

Electron density can be determined from a number of optical techniques. Stark broadening is a mechanism whereby atoms interact with surrounding charged particles resulting in a broadening of the atom's spectral lines. The energy levels of the emitting atom are perturbed by collisions with electrons (or ions). The resulting profile is a function of electron density, and to some extent, electron temperature. While no equilibrium assumptions are necessary for this technique, practical considerations limit its use to low temperature/high density plasmas[6]. The most accurate theoretical calculations are for the hydrogen Balmer lines. At electron temperatures of about 1.5 electron volts (eV) and above, however, dissociation limits hydrogen's use. Also, the halfwidths of most lines become too small to accurately measure at densities lower than about 10^{15} particles/cm^3. Nevertheless, it is possible this technique can be quite accurate. Data taken from the H_β line permit an accuracy of 5%[7].

Another technique for estimating electron density is to use an absolute continuum intensity measurement. Continuum radiation is due to two processes: Bremsstrahlung (free–free electron collisions) and photo–recombination collisions[8]. Generally speaking,

these are functions of electron density and temperature. In the visible region, the effect of temperature is negligible. One can thus relate the continuum intensity to electron density. One drawback of this technique is the necessity of an absolute intensity calibration. Additionally, spectral line wings extending into the continuum can introduce sizable errors into the measured intensities.

The refractivity of a plasma is nearly a linear function of the various specie densities present within it[9]. The deviation from unity of the refractive index can be related to these densities. Extracting a specific species density from this measurement, however, can be difficult. Also, for low densities, the actual deviation can be quite small and difficult to measure. Finally, an interferometric system would be necessary to measure the index of refraction and it is hard to imagine such a system that would be capable of acquiring more than a single data point per shot.

Thomson scattering offers yet another mechanism for measuring electron density as well as electron temperature. Electrons are capable of scattering photons that are directed at them. The intensity of scattered light as a function of scattering angle is dependent on both the electron's density and temperature and can thus be used as a diagnostic tool. In fact, Michels and Sigman[10] at NASA Lewis in 1971 made such a measurement on a nitrogen fed applied field MPD thruster. In 1972, Michels[11] presented additional data for both self field and applied field cases. Thomson scattering has the decided advantage of not requiring an equilibrium assumption. It does have some inherent disadvantages. Only a single temporally and spatially resolved data point can be obtained in a shot. To fully characterize the plasma, a great many time–consuming shots would be necessary. Additionally, the technique cannot be extended to obtain the heavy particle temperature thus failing the single system requirement set forth earlier.

Finally, the density of ions and neutrals can be determined from absolute line intensity measurements. The absolute line intensity is determined by atomic constants, geometry, and the density of atoms in the upper state of the line being observed[12]. If the

distribution of densities among all energy levels of the atom can be considered Maxwellian and their temperature is known, the total species density may then be inferred. The essential drawback of this method is the requirement of complete equilibrium within the atom. In a transient, low density MPD plasma this condition may or may not be met. This point will be investigated in considerable detail in chapter two.

1.2 Temperature measurements

The most straightforward measure of electron temperature is the relative line intensity method. If one is willing to assume that the upper level densities are in equilibrium (that is governed by a Boltzmann distribution) wherein the free electron collisions govern the transition rates then the ratio of two line intensities is only a function of atomic constants and electron temperature. Two disadvantages of this method are the generally large uncertainties in atomic transition probabilities and the often tenous assumption of equilibrium. In recent years, increasingly accurate measurements of transition probabilities has alleviated the first concern somewhat. The second concern, however, must be addressed with the specific plasma in mind.

As mentioned earlier, Thomson scattering provides another method to measure electron temperature. All of the problems discussed earlier, however, still hold.

A third technique, based on the second–order Stark effect is available. While the primary effect of Stark broadening is a dispersion of emissions, a secondary effect is a small shift in the line center. Depending on the particular line and the temperature, this shift can be an extremely sensitive measure of electron temperature. In fact, the ratio of shift to width is independent of electron density and can directly yield electron temperature. Unfortunately, typical shift to width ratios are on the order of 0.1 and, hence, require a high wavelength resolution. Burgess and Cooper[13,14] describe the method and an experimental procedure to perform it. Accurate temperature determinations require

detailed theoretical calculations of these shift to width ratios. Unlike the situation of the Balmer lines in Stark broadening where such calculations exist, second–order Stark effect theory needs more development.

Heavy particle temperatures are notoriously more difficult to measure. A standard technique relies on Doppler broadening. Random thermal motion of an atomic emitter will shift its emission frequency through the Doppler effect. Observing a large assemblage of particles results in an overall Gaussian line profile with the half–width parameter depending on temperature, frequency, and atomic weight. This method has does not require equilibrium of the species. Simple and accurate interpretation of the line profile does assume a Maxwellian distribution function although the method is still useful even when this is not the case. While this approach has a simple theoretical basis, it is difficult to use in practice. Other broadening mechanisms such as Stark broadening, microturbulance, and even a directed velocity distribution can compete and even overwhelm Doppler broadening. Additionally, Doppler widths for heavy particles such as argon are on the order of 0.05 Angstroms or less for the suspected conditions inside an MPD thruster which necessitates an extremely high wavelength resolution. Although it is a difficult diagnostic technique, its simplicity makes it extremely appealing.

One other technique for heavy particle temperature is available. The rotational temperature of a molecular system is closely coupled with the translational temperature. Even the extreme conditions in an MPD plasma allow the two modes to remain in equilibrium. Essentially, the rotational mode equilibrates with the translational mode about as quickly as the translational mode itself equilibrates. This feature can be exploited to estimate the heavy particle temperature. The spectral lines within a vibrational band of a molecular spectrum are the results of transitions between rotational modes. The relative intensity of these lines is largely a function of rotational temperature. Hence, if a plasma is cool enough to permit significant molecular densities, one can measure the appropriate relative intensity and therefore obtain an estimate of the heavy particle temperature. This

has been done in a nitrogen plasma by Robinson and Nicholls[15]. They report the method usable up to about 10000 Kelvin where N_2 is no longer present in appreciable amounts. The usefulness of this method in an MPD plasma remains to be proven. Estimates of the heavy particle temperature range from a few thousand degrees up to nearly 50000 degrees. As such, any estimate of temperature would be useful. By seeding MPD plasmas with appropriate molecular traces, investigators may find this method preferable to a Doppler technique.

1.3 Selected techniques

Specifically, this investigation focused on measurements of electron density, electron temperature, and heavy particle temperature in an MPD plasma. The requirements of spatially and temporally resolved optical data acquisition necessitated the use of an optical multichannel analyzer (OMA) system with a silicon intensified vidicon detector. This system was chosen because it fulfilled all the aforementioned requirements. Defining the operating characteristics of the apparatus turned into an essential feature of the investigation. In fact, equipment limitations largely dictated the success of the measurement techniques that were used.

Electron temperature was measured with the relative line intensity method. The equilibrium assumption was quantified and explored with the use of simple models for the various rate processes taking place in the plasma. One conclusion was that the typical local thermodynamic equilibrium assumption necessary for this measurement is less stringent than expected. Measurements with and without time resolution were made and compared. The results indicated that time resolved measurements are critical for proper characterization of the flow.

Electron densities were measured through Stark broadening of the H_α line in the Balmer series. An interesting problem arose when the ionization fraction was found to be

close to unity. The plasma temperature was high enough to ionize nearly all of the hydrogen in the argon plasma. As such, H_α was the only detectable hydrogen line and the more desirable H_β line was not available. Interpretation of the observed line profile was not straightforward and some discussion is dedicated towards exploring that interpretation. As a further check on the Stark broadening technique, emissions from a dense plasma jet (a device with a quite different geometry and operating condition) were observed. In this case, the measurement was completely successful due to greater hydrogen intensities and line widths.

Three attempts were made to determine the heavy particle temperature. Doppler broadening was explored but resolution limitations of the vidicon detector would not permit sufficiently resolved argon profiles. This limititation could be overcome with additional equipment. The nitrogen based rotational temperature technique was then tried but the necessary lines were not observed. The system response in the ultraviolet was unexpectedly low thus precluding observations of the necessary lines. Once again, additional equipment can overcome this problem. Finally, a method based on a deconvolution of a mixed Stark and Doppler profile was tried. This technique, described in chapter two, proved fruitless as only H_α was observable while at least two Balmer lines were required. This method has considerable promise for future application.

The final data acquisition system along with the chosen optical techniques proved able to satisfy the diagnostic requirements set out earlier in the chapter. The operating conditions within the MPD thruster chosen as the subject of these diagnostics substantially decreased the effectiveness of the techniques. Nevertheless, the potential application of this comprehensive diagnostic tool to other MPD thrusters was clearly demonstrated.

CHAPTER 2

Theoretical analysis

2.1 Introduction

The theoretical basis of the diagnostic techniques employed in this experiment are well over 20 years old. They have been used in countless experiments including numerous studies of MPD thrusters. The application of these basic techniques, however, is what makes the approach in this thesis unique. Extensive digital signal processing, simple mathematical reformulations and unprecedented spatial and temporal resolution contribute to this unique character. The result is an instrumental and analysis package capable of rapidly and accurately characterizing a plasma. The necessary theory is divided into three areas: signal processing, relative intensities, and line broadening.

2.2 Digital signal processing

The acquired data must be processed in two ways: noise filtered and mathematically unfolded through an Abel inversion. Both the silicon intensified (SIT) camera response and plasma fluctuations contribute to a high spatial frequency component in the data. In fact signal to noise ratios can be as low as three for some measured spectral lines. Extracting meaningful data in these circumstances requires careful noise filtering. The observed intensity from an axially symmetric optically thin plasma discharge (such as the one used in this study) is comprised of emission coefficient contributions from cylindrical layers within the plasma. The well known Abel's inversion allows recovery of the radial distribution of emission coefficient from the intensity observed by looking at the plasma at right angles to the axis of symmetry. There are numerous techniques available for both of these processing requirements.

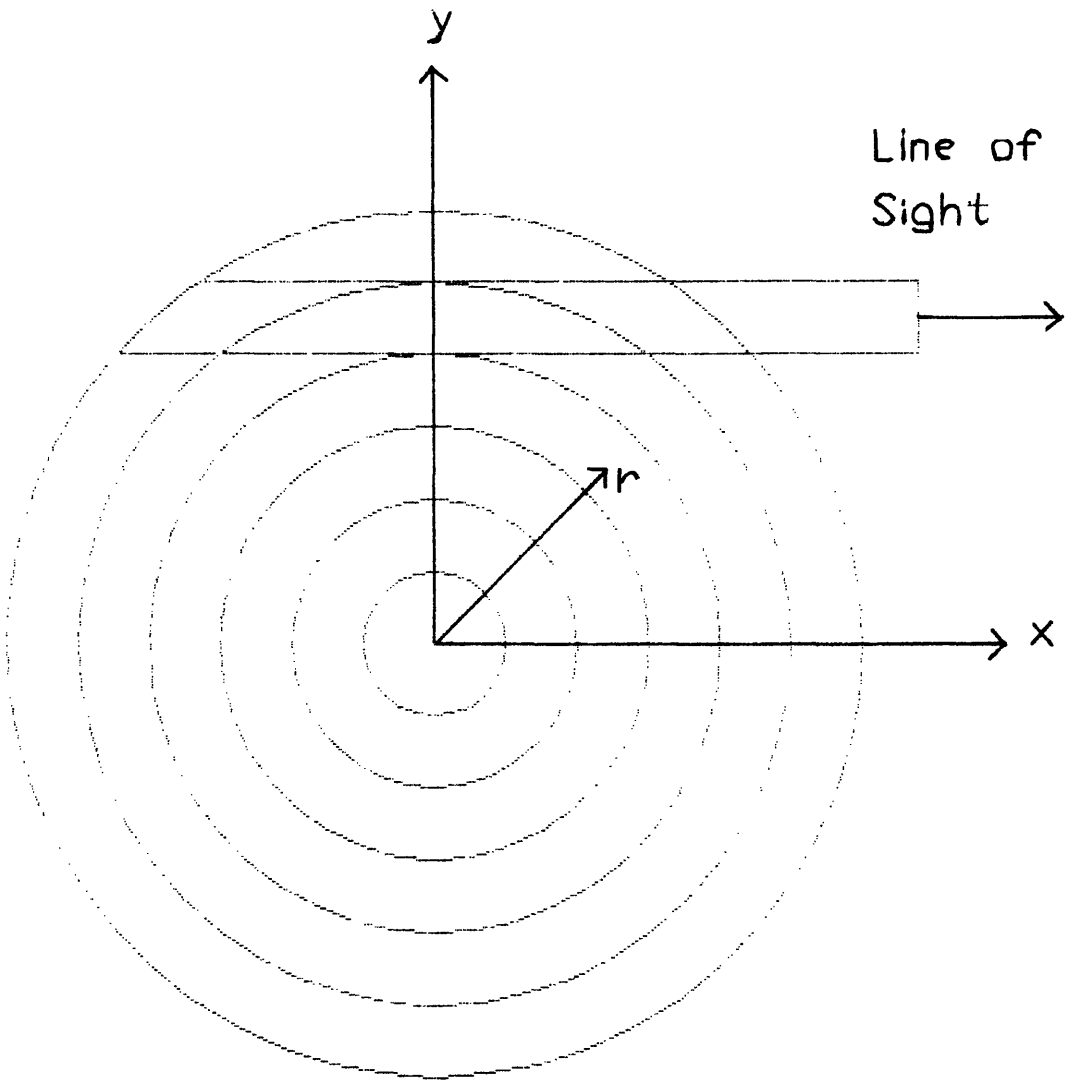

Figure 2.1. Illustration of variables and geometry used in an Abel inversion.

The formulation of the Abel inversion is straightforward[16]. With reference to figure 2.1, the x,y–axis define the observation plane and the z–axis defines the axis of symmetry. If one is observing in the x–direction, then the observed intensity (per steradian), I(y), is related to the emission coefficient, $\epsilon(r)$, by equation 2.1.

$$2.1 \qquad I(y) = 2\int_0^{\sqrt{R^2 - y^2}} \epsilon(r)\, dx = 2\int_y^R \frac{\epsilon(r)\, r}{\sqrt{r^2 - y^2}}\, dr \quad \text{where R = outer radius}$$

This integral can be solved analytically resulting in the following expression for the emission coefficient.

$$2.2 \qquad \epsilon(r) = -\frac{1}{\pi}\int \frac{dI(y)}{dy}\frac{dy}{\sqrt{y^2 - r^2}}$$

Two features make this integral unsuitable for direct application. First, small errors in the measured quantity I(y) can generate substantial errors in its derivative. This drawback cannot be overcome as it is inherent in the nature of the solution. Proper noise filtering can offset this problem. Secondly, the integrand is singular at the lower limit. This feature poses problems for most numerical approaches to the solution. There are a number of solution techniques that have been taken and several are listed here.

1) Graphical integration

2) Expansion of equation 2.1 into a set of linear equations to be solved with matrix techniques.

3) Analytically evaluating equation 2.2 by fitting an n^{th} order polynomial to the observed intensity.

Method 1 is certainly too tedious to consider. Method 2 tends to accumulate errors during the analysis and also becomes time consuming if large matrices are evaluated. Both of this methods have difficulty dealing with the singularity. Method 3 has been implemented in a number of ways ranging from a single polynomial fit to dividing the data into smaller regions and fitting each region independently. Cremers and Birkebak[17] discuss a number of these methods while Berge and Richter[18] also give a lengthy discussion. All of these

methods are plagued by tedious error calculations, large processing time requirements, and smoothing routines with undetermined filter characteristics. Keefer, Smith, and Sadharsanan[19] give an alternative using integral transforms with none of the above drawbacks.

The reformulation begins with equation 2.1 written slightly differently.

$$2.3 \qquad I(y) = \int_{-\infty}^{\infty} \epsilon(\sqrt{x^2 + y^2}\,)\, dx$$

The one dimensional Fourier transform of equation 2.3 is:

$$2.4 \qquad FT[I(y)] = \int_{-\infty}^{\infty}\int_{-\infty}^{\infty} \epsilon(\sqrt{x^2 + y^2})\, \exp(-j2\pi yq)\, dy\, dx$$

By changing the variables of integration from cartesian to polar coordinates, it can be shown[20] that:

$$2.5 \qquad FT[I(y)] = 2\pi \int_{0}^{\infty} r\,\epsilon(r) J_0(2\pi rq)\, dr$$

J_0 is the zero order Bessel function of the first kind. The right hand side of equation 2.5 is the zero order Hankel transform of $\epsilon(r)$. Thus, the radial emission coefficient can be found by taking the inverse Hankel transform of the Fourier transform of $I(y)$.

$$2.6 \qquad \epsilon(r) = 2\pi \int_{0}^{\infty} qJ_0(2\pi rq) \int_{-\infty}^{\infty} I(y)\exp(-j2\pi yq)\, dy\, dq$$

This formulation has no difficulty with the original singularity. Filtering can be employed in the Fourier domain in a determined manner. Also, both transforms can be performed numerically via the fast Fourier transform algorithm thereby substantially decreasing the required computation time. Candel[21] presents an algorithm for calculating the Hankel transform using the fast Fourier transform. Keefer, et. al.[19], also demonstrate a technique whereby the symmetry axis can be determined from the data. For these reasons, this processing technique was chosen to perform the Abel inversion. As a simple demonstration of the accuracy of the technique, Figure 2.2 graphically shows the Abel inversion of an

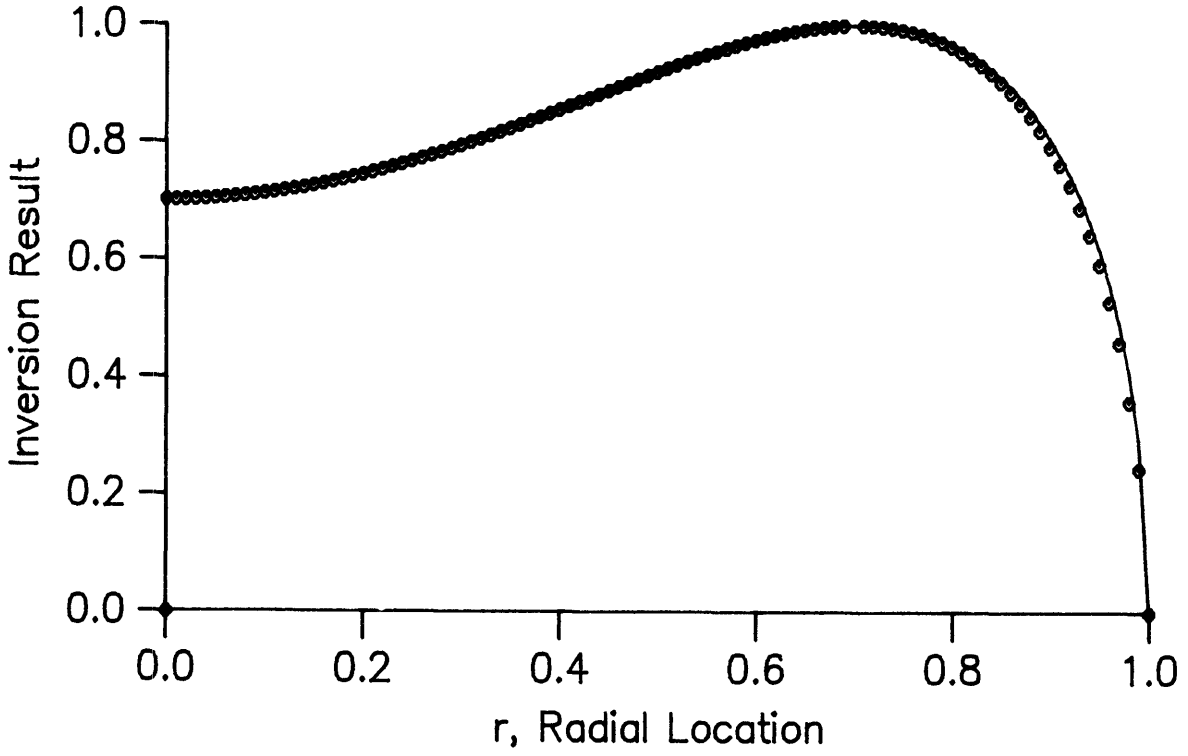

Figure 2.2. Abel inversion of $1-y^4$. The solid line is the analytical result and the symbols are the numerical result.

intensity distribution of the form, $1 - y^4$. The solid line is the analytical solution and the symbols represent the transform result using discrete values of I(y).

The issue of error propagation through the Abel inversion is addressed by Smith[22]. Assuming the signal noise to be a wide sense stationary random process, he found the resultant mean of the radial noise to be zero. Since the original noise is stationary with constant mean, its derivative has zero mean. A simplified expression for the output variance was found by assuming the original noise is band limited such that its spectral power density is given by:

2.7 $$G_n(f) = \begin{cases} \frac{\sigma^2}{2B} ; |f_n| < B \\ 0 \quad ; |f_n| > B \end{cases}$$; B.= bandwidth of noise

In this case this case, the output variance for values of $2\pi rB > 1$ is approximately equal to $\sigma^2 B/4r$ (where σ^2 = variance of original noise). Just to gain a sense of the magnitudes involved, assume a constant emission coefficient, ϵ. Then, from equation 2.1:

2.8 $$I(y) = 2\epsilon\sqrt{R^2 - y^2} \approx \epsilon R$$

Thus, the ratio of error before inversion to error after inversion becomes:

2.9 $$\frac{\sigma / I}{\sqrt{B/2R}\ \sigma/\epsilon} = \sqrt{2/RB}$$

For much of this analysis, a lowpass filter of bandwidth, B = 0.05 cycles/data point, was used and the radius, R, was approximately 80 data points. Therefore any noise present in the data was limited to a spatial frequency of 0.05 cycles/data point. With these values, the inverted relative error was about one and a half times greater than the original error. The importance of properly filtering data prior to inversion is made clear by this point.

As a demonstration of the noise handling capabilities of this method, a numerical experiment was performed. The test function, $1-y^4$, had normal Gaussian noise with zero mean and 0.2 variance superimposed on it. Figure 2.3a shows the test function with superimposed noise. Figure 2.3b shows the result of simply Abel inverting the noisy function. The result is clearly nonsense. Figure 2.3c shows the Abel inversion of the smoothed test function. Even with a 20% noise fluctuation, the analysis yields a solution accurate to 10% through much of the profile.

The final point to be addressed in this section concerns the possible absence of data below a certain value, y_{min}, for $I(y)$. Equation 2.2 reveals that the emission coefficient at a radial location, r, is only a function of the observed intensity for values of $y \geq r$. Thus, one need only record data for values of y greater than the minimum radius for which the emission coefficient is sought. In the transform technique, however, the integrals have domains that span all space. Since equations 2.2 and 2.5 are mathematically equivalent,

$\epsilon(r)$ should have the same property in both cases. Unable to analytically confirm this, a numerical test was performed using an observed intensity distribution of the following form.

$$2.10 \qquad I(y) = \begin{cases} I(y_{min}) & ; 0 \le y \le y_{min} \\ 1 - y^4 & ; y_{min} \le y \le 1 \end{cases}$$

Figure 2.4 clearly shows that the transform result closely matches the analytical result for $y \ge y_{min}$ even though the input data below this value was incorrect.

The preceeding procedures were performed with the aid of the ASYSTANT$_{tm}$ software package created by Macmillan Software Company.

2.3 Relative line intensity method

The relative line intensity method for determining electron temperature relies heavily on a local thermodynamic equilibrium (LTE) assumption. When LTE prevails, the densities in certain quantum states of a system correspond to those of a system with the same mass, density, temperature, and chemical composition that is in complete equilibrium. The temperature that describes the distribution among these states corresponds to the distribution function of the species which governs the reaction rates. For dense plasmas with electron densities higher than approximately 10^{22} m^{-3} this condition is often met for at least the highest quantum numbers of a given ion. For MPD's, with densities often lower than 10^{22} m^{-3}, the LTE assumption is questionable. The validity of the assumption in this case will be discussed later.

Robinson and Lenn[23] develop the relevant equation for the relative line intensity method as follows. The absolute intensity of a spectral line (in $eV/sec/m^3$) generally is given by:

$$2.11a \qquad I_{mn} = \frac{A_{mn}(E_m - E_n)g_n N_i}{Q}$$

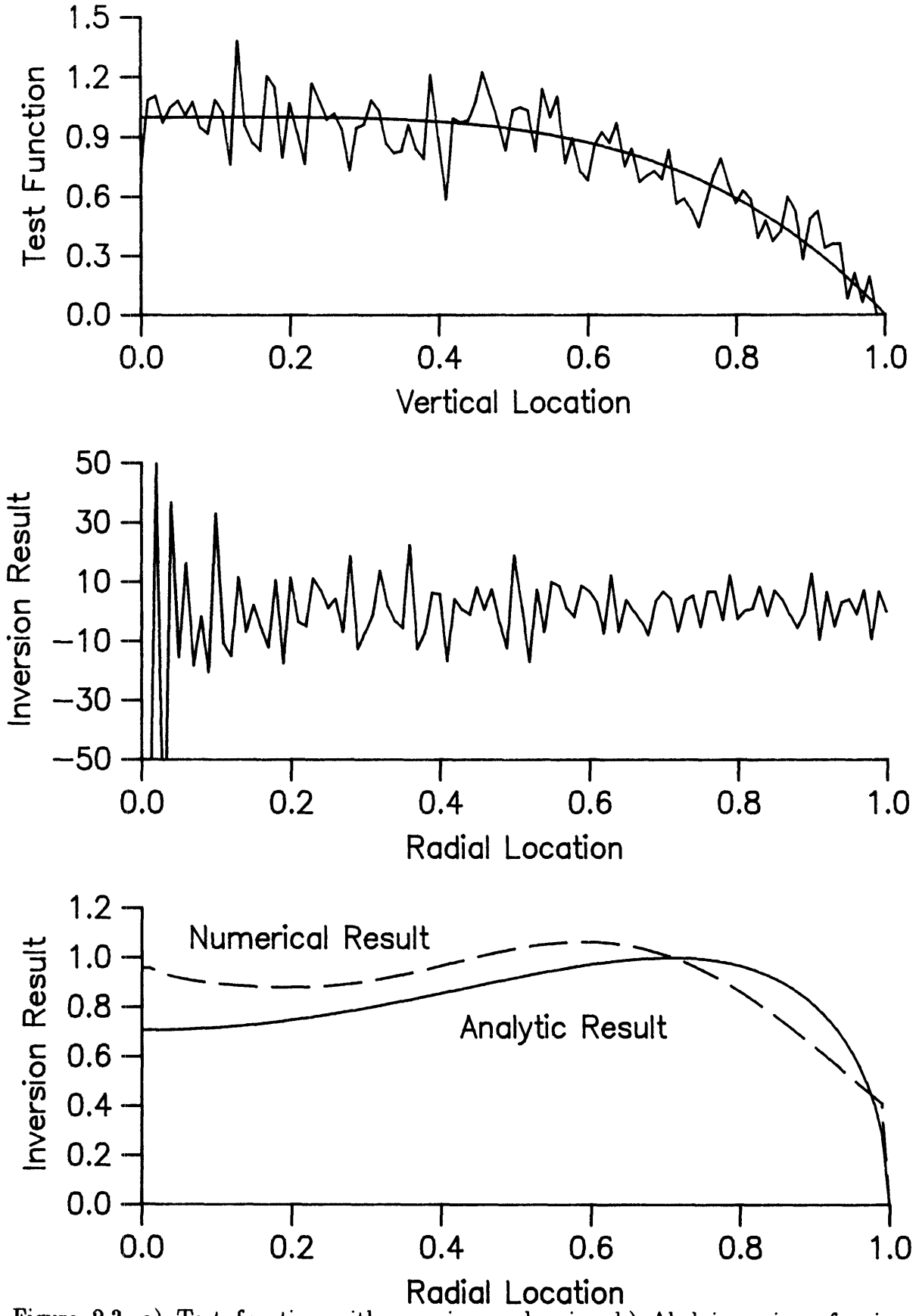

Figure 2.3. a) Test function with superimposed noise. b) Abel inversion of noisy test function. c) Abel inversion of smoothed noisy test function

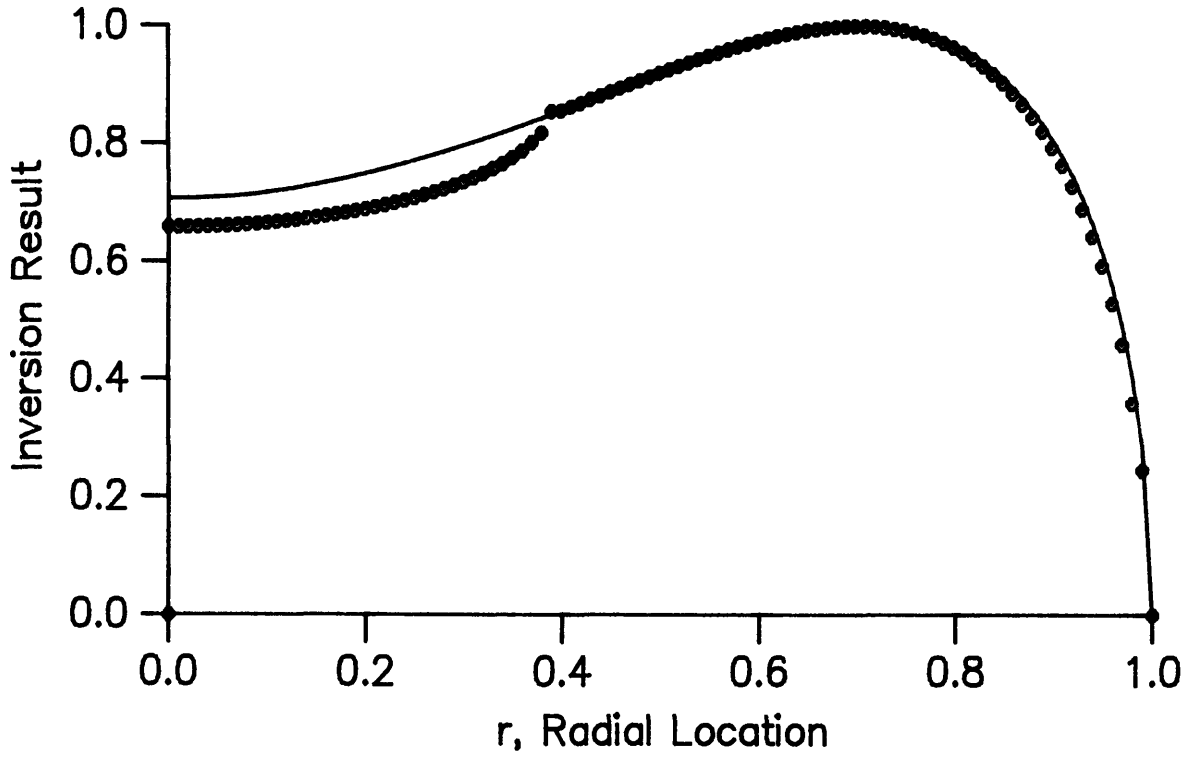

Figure 2.4. Effect of bad data below a certain radius. The solid line is the analytical result and the symbols represent the numerical result.

2.11b $$= \frac{A_{mn}(E_m - E_n)g_n N}{Q} \exp(-E_m / T_e)$$

Where: A_{mn} = transition probability [sec^{-1}]
E_m, E_n = energy of upper and lower states [eV]
g_n = statistical weight of lower state
N_i = number density of species in state i [m^{-3}]
N = number density of species [m^{-3}]
Q = partition function
T_e = electron temperature [eV]

In going from equation 2.11a to equation 2.11b, use has been made of the well known statistical mechanics relationship between total density and state density which is only valid when thermodynamic equilibrium prevails. Defining the oscillator strength, f, and taking the intensity ratio of two lines from the same species (noting that **Q** and **N** are the same for each transition), the following equation is arrived at:

$$2.12 \qquad \frac{I_1}{I_2} = \frac{\left[\frac{g_1 f_1}{\lambda_1^3}\right]}{\left[\frac{g_2 f_2}{\lambda_2^3}\right]} \exp\left\{\frac{-(E_{m1} - E_{m2})}{T_e}\right\}$$

Where: $f_i = 1.5 \times 10^{-16} \lambda_i^2 A_{mn}$
λ_i = wavelength [Angstroms]

If the intensity ratio is divided by the exponential coefficient and the natural logarithm taken of both sides, the equation takes the form of $y = bx$ where x is the difference in upper level energies and the slope is equal to $1/T_e$. This graphical technique is known as a Boltzmann plot. Typically one measures the intensities of several transitions and performs a linear regression to extract the electron temperature.

2.3.1 Error analysis

In order to guide the choice of lines, a brief error analysis is helpful. The ratio that appears on the y–axis of the Boltzmann plot contains four parameters: I, λ, g and f. Typically, λ and g are known with high accuracy. If the relative uncertainty in the intensity measurements, ΔI, is constant and the relative uncertainties in the two oscillator strengths, Δf_1 and Δf_2, are known, then the relative uncertainty in the calculated electron temperature is:

$$2.13 \qquad \Delta T_e = \pm (2\Delta I + \Delta f_1 + \Delta f_2) \frac{T_e}{\Delta E} \ [\%]$$

For this example, based on a single measurement, two guidelines are indicated. First, choose as large an energy difference, ΔE, as possible. Secondly, choose lines with as precisely known oscillator strengths as possible. An additional element to consider is the effect of increasing the number of measurements. The standard deviation of a slope found by linear regression is related to the standard deviation of the measured y–values by[24]:

$$2.14 \qquad \sigma_{slope} = \sigma_y \frac{1}{\sqrt{n}\, S_x}$$

Where: σ = standard deviation
n = number of data points

$$S_x^2 = \frac{1}{n}\left[\Sigma x_i^2 - n(\overline{x})^2\right]$$

Thus, the uncertainty in the electron temperature goes down with the square root of the number of data points. The uncertainty with three measured spectral lines is approximately 60% of the uncertainty with two measured lines. A final guideline is then to record as many lines as possible. It should be noted that this error reduction is based on the assumption of completely random errors. If there is a systematic error, additional data points will not reduce its effect.

2.3.2 Validity of LTE assumption

While there are numerous types of equilibrium, the relevant definition for this method is that the population distribution of the atomic energy levels used in the measurement must be in thermal equilibrium with the free electrons. This will be true if the collisional transitional rates in the levels are much greater than any non–equilibrium process rates such as radiation or fluctuations in species density and temperature due to diffusion and advection/convection. The complete rate equations for a non–hydrogenic plasma are complex, coupled, and non–linear. For the sake of gaining some insight, one can, however, construct approximate expressions for the rates in a hydrogenic system and evaluate them individually. The rates of radiative transitions, ambipolar diffusion recombination, three body recombination and, to some extent, convection will be considered. One point should be emphasized. These calculations are extremely approximate and will serve only to raise confidence in an LTE assumption, not to prove it.

The case of radiative transitions in competition with collisionally induced transitions is treated by Griem[25], Mitchner and Kruger[26], and Wilson[27]. Typically, lower lying atomic levels have shorter radiative lifetimes than the higher lying levels. Thus, there is a trend of decreasing radiative rates as the principal quantum number increases.

Collisional rates, however, exhibit the opposite trend. Transitions in the lower lying levels involve relatively large energy jumps. This leads to small collisional cross–sections and, hence, small collisional rates. Collisional transitions, then, increase with principle quantum number. In an optically thin plasma, this leads to an underpopulation of the lower energy levels and a departure from a purely thermal distribution. In line with Wilson's reasoning, one introduces the concept of a thermal limit. The limit is an energy level, above which, population distributions are governed by collisional rates. Wilson's definition is "the level at which upward and downward transitions are equally probable." Physically this means that higher lying levels are in better communication with what is above them while lower lying levels communicate mostly with what is below them. He arrives at the following expression to define this limit.

$$X_t = 1.26 \times 10^{-5}\, X_i\, z^{-12/7} \left[\frac{n_e^2}{T_e}\right]^{1/7} \qquad 2.15$$

Where: n_e = electron density in cm^{-3}
z = nuclear charge
X_i = ionization potential [eV]
X_t = ionization potential of the thermal limit [eV]

This thermal limit is plotted for singly ionized argon for a range of plasma conditions in figure 2.5. The plot shows that a thermal limit of 5 eV can be expected for a plasma with a density of 10^{16} cm^{-3}. Some account is made for a general (not hydrogen) ion by accounting for the actual ionization energy and nuclear charge. Having no idea of what modification a non–hydrogenic ion system would require, one can simply hope that this expression is valid. One reasoning for generalizing this result's applicability is given by Griem. For large principal quantum numbers, most transitions are into nearby excited levels. The influence of a complex ground state structure is felt less strongly in these high excited levels and, thus, one might assume a hydrogen–like behavior. This is hardly a quantifiable statement but, again, it does raise confidence in the assumptions. In order to compare all the relevant

transition rates, simple models must be adopted. For a hydrogenic atom, the radiative transition rate is given by Griem.

$$2.16 \qquad R_n = 1.6 \times 10^{10} \frac{z^4}{n^{-9/2}} = 1.6 \times 10^{10} z^4 \left[\frac{X_t}{X_i}\right]^{9/4} [sec^{-1}]$$

Where: n = principle quantum number

The substitution for n is based on Bohr's atom relationship: $n^2 = X_i/X_t$. Griem developed an expression for the collisional transition rate between upper lying levels in an atom:

$$2.17 \qquad C_n = \frac{9 \times 10^{-8}}{4\ z^3} N_e\, n^4 \left[\frac{z^2 X_h}{T_e}\right] [sec^{-1}]$$

Where: X_h = ionization potential of hydrogen [eV]

The remaining reaction rates can be classed as depopulating effects. Ambipolar diffusion, recombination, and advection all have the effect of eliminating particles from the system. If particles are eliminated before they can undergo enough collisions to equilibrate, any equilibrium assumption will be inaccurate. Although these processes do not initiate inter–level transitions they must nevertheless be accounted for. Appendix 1 contains a description of the models used to arrive at the following approximate rate equations. The rate of depopulation due to ambipolar diffusion for singly ionized argon can be estimated by:

$$2.18 \qquad D = \frac{1.31 \times 10^{15} \sqrt{T_e}}{L^{2\frac{1-\alpha}{\alpha}}\, n_e} \quad [sec^{-1}]$$

Where: L = half the characteristic length [m]
α = ionization fraction, n_e/n_t

Following the development of Mitchner and Kruger, the depopulation rate due to three body recombination can be estimated by:

$$2.19 \qquad R_3 = 1.11 \times 10^{-26}\, T_e^{-9/2}\, n_e^2 \ln \Lambda \ [sec^{-1}]$$

Where: Λ = a tabulated function of T_e

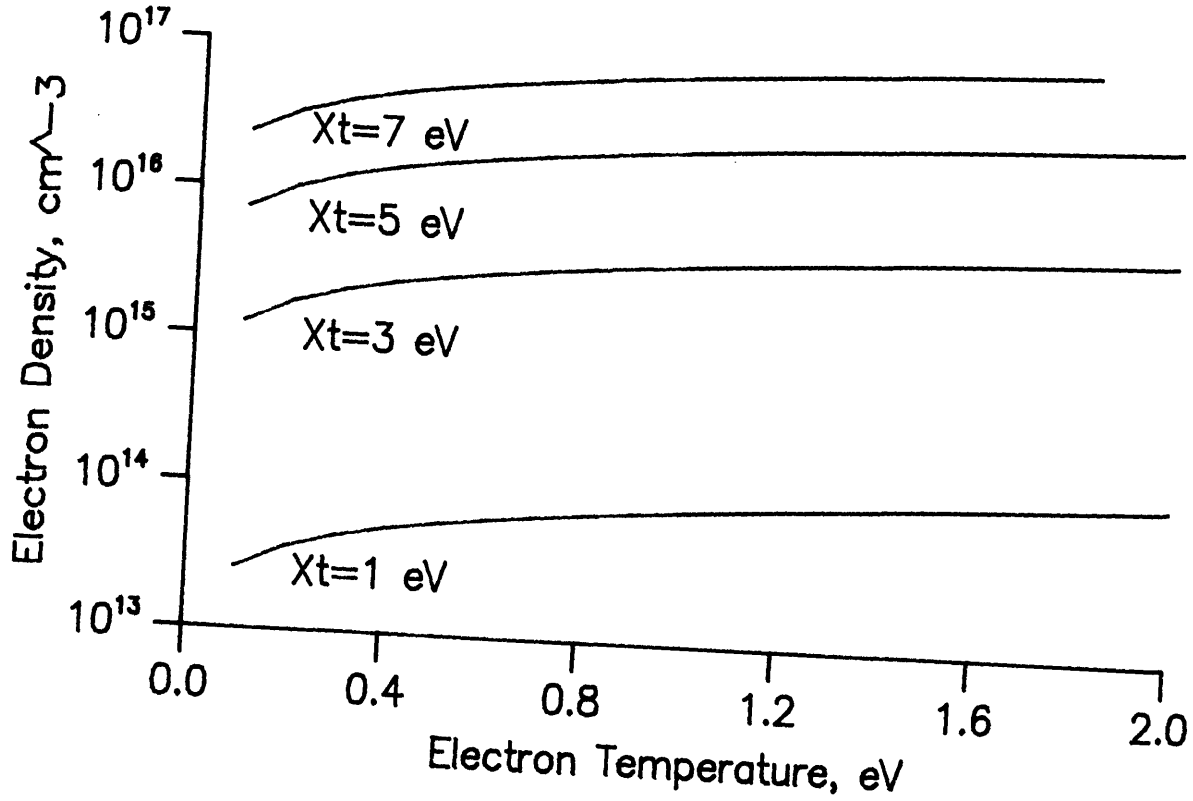

Figure 2.5. Wilson's thermal limit for ArII in a range of plasma conditions.

Finally, the advection rate can be simply estimated by:

$$A = V/L \ [sec^{-1}] \qquad 2.20$$

Where: V = a characteristic velocity

For a range of anticipated conditions in the MPD treated in this work, all these rates are plotted in Figure 2.6. In the vicinity of $n_e = 10^{15}$ cm^{-3} (a typical operating regime), all of the depopulating mechanisms are of similar magnitude. While this is disheartening for any generalized plasma fluid models, the LTE assumption for a relative intensity measurement is clearly unaffected by these mechanisms (within the limits of the assumptions made...) as the collisional transition rate is several orders of magnitude higher. The conclusion of all this analysis is simple. The LTE assumption depends mainly on the radiative versus collisional transition balance. Quantitatively, this analysis suggests that the lines used in

an electron temperature measurement with singly ionized argon should lie within 5 electron volts of the ionization limit.

2.4 Line broadening

A number of mechanisms are known to broaden spectral lines. In situations where one or more mechanisms dominate one can infer certain plasma properties from the line profiles. This investigation will focus on one particular broadening theory, Stark broadening, and briefly discuss possible applications of another, Doppler broadening.

2.4.1 Stark broadening

W.L. Wiese[28] gives a comprehensive discussion of line broadening theories. Stark broadening is a sub–class of the more general theory of pressure broadening whereby the line profiles of an emitter are determined by interactions with surrounding particles. In plasma with electron densities greater than about 1% of the total density, Stark broadening dominates over the other mechanisms. Historically, two extreme approximations have been used to describe Stark broadening. In the impact approximation, one models the emitter as continuously emitting a wave train that is periodically perturbed by an instantaneous collision and essentially cut into a number of smaller segments. Fourier analysis and statistical averaging of these smaller segments yields an expected intensity distribution over wavelength which can be closely approximated by a Lorentzian profile. The quasi–static approximation assumes a continuous perturbation of the emitter. The perturbation is assumed constant over the time of emission. This approximation is suitable for the slowly moving ions as perturbers while the impact approximation is appropriate for the electrons. More detailed analysis of these theories can be found in Lorentz[29], Kolb and Griem[30], and Holtsmark[31]. Currently, there is a quantum mechanical approach to the impact approximation that includes quite a number of complex features. For the experimentalist, however, one need only know that halfwidths as a function of electron

density (and to some extent temperature) are tabulated for a wide range of lines. Figure 2.7 gives the full widths at half maximum for the two important lines used in this study, H_α (6562.8 Å) and H_β (4861.3 Å), as a function of electron density.

2.4.2 Doppler broadening

Doppler broadening is caused by the random thermal motion of the emitters. Each emitter in a plasma emits at a Doppler shifted frequency where the shift is related to the emitters velocity along the line of sight. The result of looking at the entire plasma is to see an apparently continuous intensity distribution in wavelength. The profile is a Gaussian and the full width at half maximum (FWHM) is given by[32]:

$$\lambda_t = 7.16 \times 10^{-7} \lambda \left[\frac{T}{\mu}\right]^{1/2} \tag{2.21}$$

Where: λ = wavelength at line center [Angstroms]
T = emitter temperature [K]
μ = atomic weight in atomic units

Typically, this FWHM is too small to accurately measure without sophisticated equipment. For argon at 10000 K the FWHM is 0.06 Angstroms. For hydrogen, the FWHM is 0.4 Angstroms. In this investigation, the diagnostic resolution was not sufficient to measure argon Doppler broadening. For hydrogen, however, the Doppler broadening was of an order that theoretically could be measured.

2.4.3 Convolution of broadening mechanisms

The simultaneous presence of Doppler and Stark broadening results in a profile known as the Voight profile, V(). This convolution is given by:

$$V(\Delta\lambda^*) = \int \mathrm{Dop}(\Delta\lambda^*)\, \mathrm{Sta}(\Delta\lambda - \Delta\lambda^*)\, d(\Delta\lambda^*) \tag{2.22}$$

Where: Dop() = Doppler profile
Sta() = Stark profile

One analytic result that can be noted is that if either mechanism independently has a FWHM less than one–third of the other, the observed line is only affected by 15–20%.

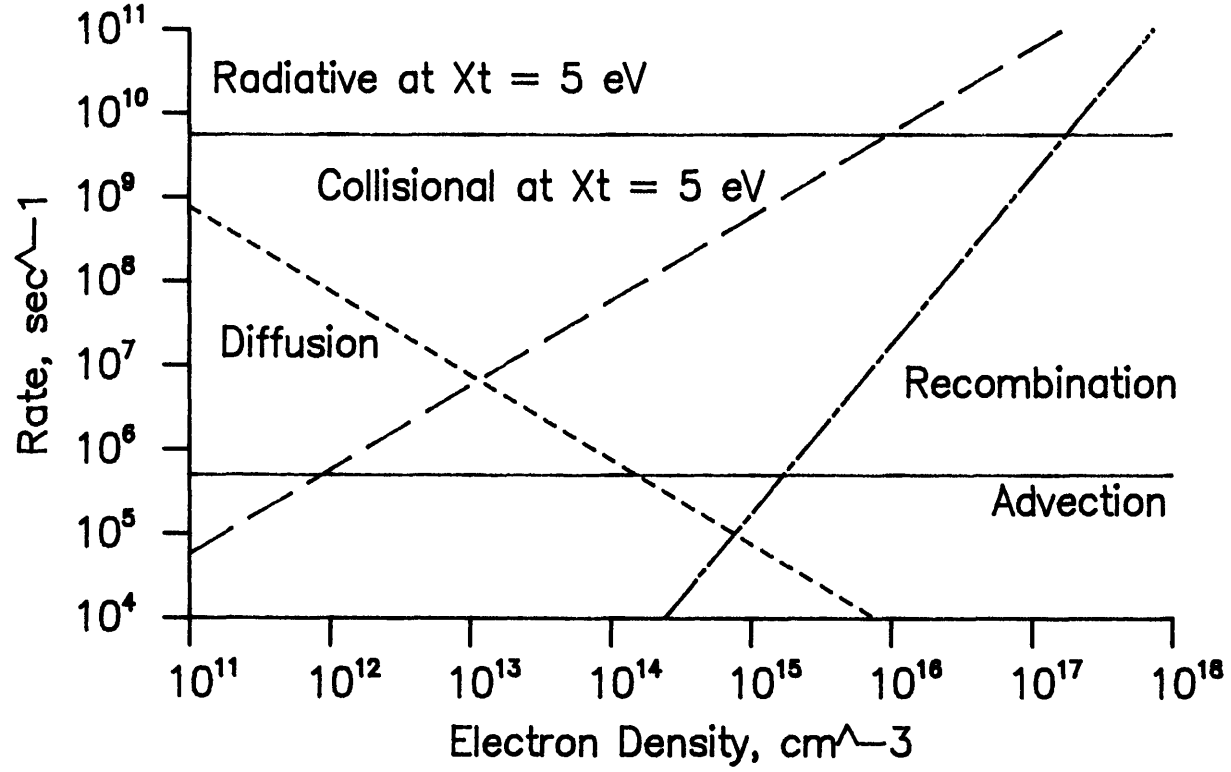

Figure 2.6. A graphic comparison of the relevant rate processes in the MPD plasma.

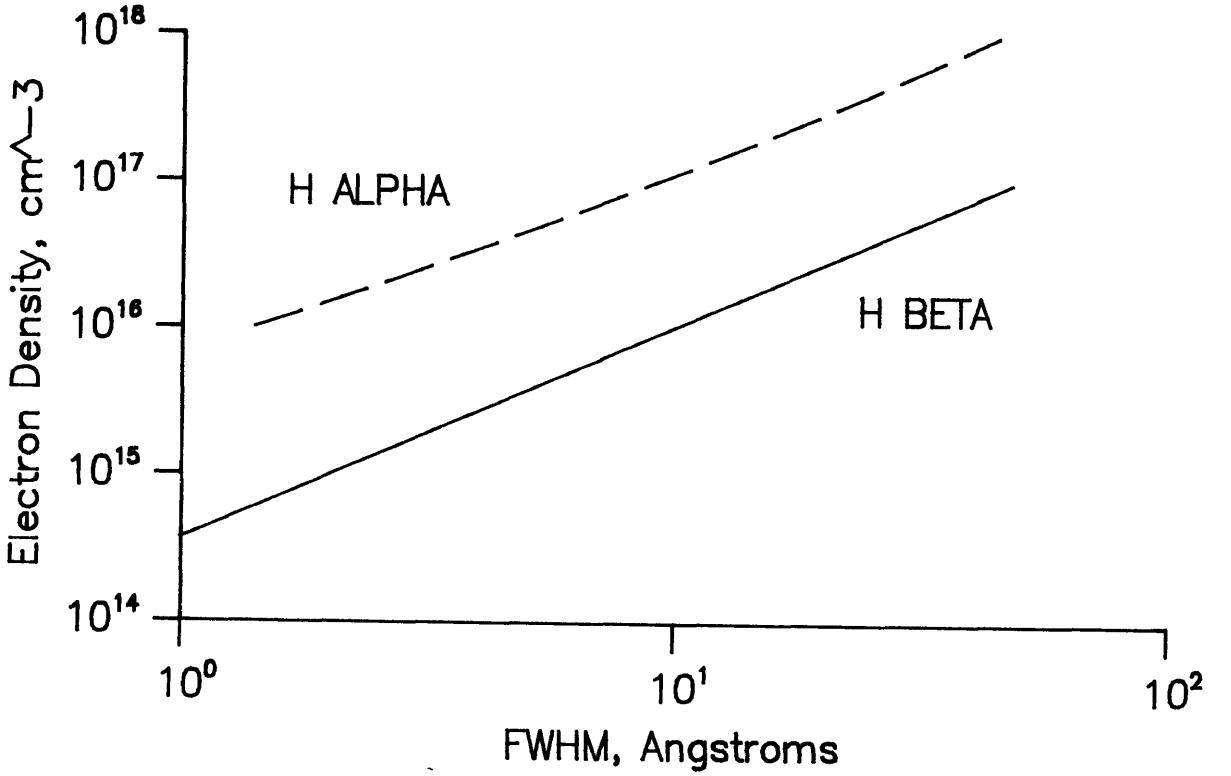

Figure 2.7. Full width at half maximum of the two Balmer lines, Hα and Hβ, for a range of electron densities.

Numerically, then, one needs FWHM's of comparable order to accurately interpret the Voight profile. The convolution presented here offers an interesting technique for calculation of the ion temperature. For most argon lines, the dominant broadening mechanism is Doppler but the FWHM is too small to readily obtain the ion temperature. Hydrogen, 40 times lighter than argon, has a significantly greater doppler width. If one could justify an assumption that the hydrogen atoms are nearly in thermal equilibrium with the heavier species (argon), then a measurement of the hydrogen Doppler width could be interpreted as a heavy particle temperature. Specifically, one could proceed as follows. Measure the electron density from Stark broadening of a line where the Doppler width is significantly smaller than the total width (such as H_β). Next, measure the profile of a line where Doppler and Stark broadening compete (such as H_α). Recalling that the convolution of two functions is simply the inverse Fourier transform of the product of their Fourier transforms, one could apply the analysis demonstrated schematically below.

$$I_{H\alpha}(\Delta\lambda) \Longrightarrow \text{Fourier Transform} \searrow$$

$$\text{Divide} \Longrightarrow \text{Inv. F. T.} \Longrightarrow \text{Doppler Profile}$$

$$I_{H\beta}(\Delta\lambda) \Longrightarrow \text{Fourier Transform} \nearrow$$

The application of this technique will be discussed in Chapter 4.

Chapter 3

Experimental Apparatus and Procedure

3.1 Introduction

The common requirement of all the chosen analysis methods are spectral line profiles from the plasma that are resolved in both space and wavelength. The desired data is a two–dimensional array with the vertical dimension corresponding to a definite spatial position in the plasma and the horizontal dimension representing wavelength. Quantitatively, the spatial resolution needs to be great enough to distinguish structure within the length scales of the plasma device. The required wavelength resolution is specified by the widths of the observed spectral lines. Again, the analysis methods require knowledge of the line profile on a wavelength scale substantially smaller than the total width. One would hope for at least ten or so data points across the profile. The apparatus necessary to make such measurements can be divided into three subsystems: the plasma generation system, the optical system, and the data acquisition system.

3.2 Plasma Generation System

While the methods and techniques described in this report will work for a variety of plasma diagnostic applications, a magnetoplasma dynamic (MPD) thruster was chosen as the source. The applicability of the data acquired to a theory being developed by Professor Manuel Martinez–Sanchez of M.I.T. and PhD candidate Daniel Heimerdinger provided the motivation for this choice. A detailed discussion of the MPD design and performance can be found in Heimerdinger's doctoral thesis. This thesis will not focus on design criteria but will rather simply specify the design chosen. A schematic of the basic components of the MPD system is given in figure 3.1

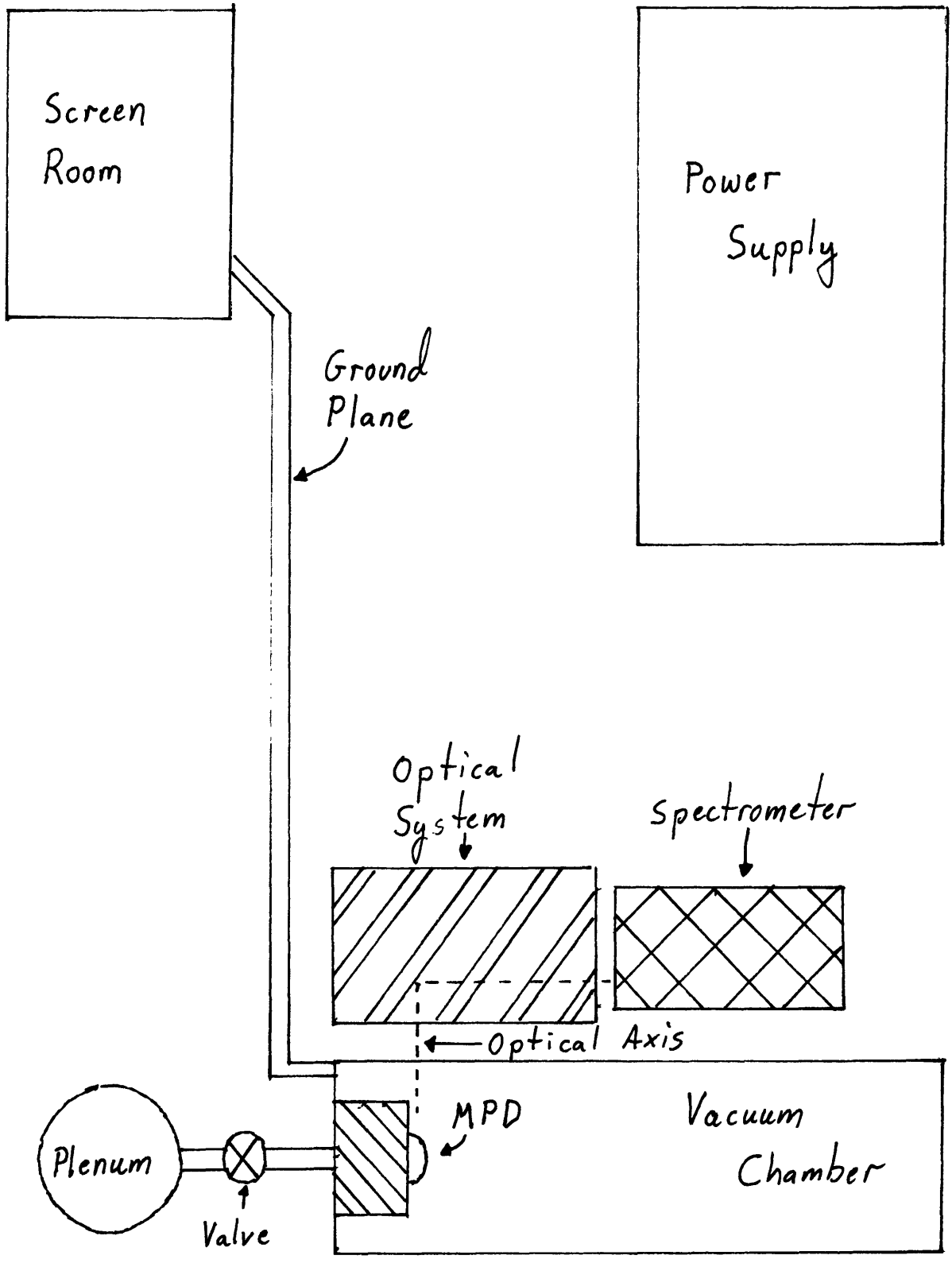

Figure 3.1. Schematic of MPD spectroscopic analysis system.

3.2.1 The MPD

The MPD itself is based on a coaxial geometry with three configurations. These variations are in the shape of the cathode and are motivated by the theory mentioned above. Each cathode is machined from copper and is hollowed out (to save weight). The hollowed area is capped with a Plexiglass plate to keep plasma and current from entering. Three cathode shapes were used: a constant radius cylinder (the constant area channel), a constant radius section followed by an inwardly flaring region downstream (the partially flared channel), and inwardly flaring sections both upstream and downstream of the throat (the fully flared channel). These three geometries are detailed in figure 3.2. Each cathode is bolted to an aluminum base which is in turn attached to an aluminum cathode sleeve.

The anode is machined from aluminum and has an exterior anodizing layer of Hardcote (2 mils thick). The anode attaches to an aluminum anode sleeve via a connector. Finally, an insulating Plexiglass flange seals the anode to the vacuum tank.

The propellant feed system begins with a gas plenum within the cathode sleeve. Connecting this plenum to a small pre–expansion plenum are six solenoid valves. These valves open in under 100 μseconds under the guidance of a valve driver circuit designed by Steve Seiler of R & D Associates, Washington Research Laboratory. These valves are fiber optically triggered. The gas leaves this plenum through a plexiglass choking plate that regulates mass flow and enters the channel through a boron nitride backplate.

3.2.2 The Vacuum system

The vacuum system consists of a 0.6 m diameter stainless steel pipe with two six inch oil diffusion pumps that keep the tank static pressure to less than 10^{-5} Torr. A number of Plexiglass portals are installed to allow optical access to the plasma.

3.2.3 The Power Supply

The power supply is essentially an inductor–capacitor (L–C) ladder network. It consists of eight stages with a total energy capacity of 400,000 Joules. Each stage is rated at 20,000 volts. The ladder is switched by a General Electric Ignitron switch. In this

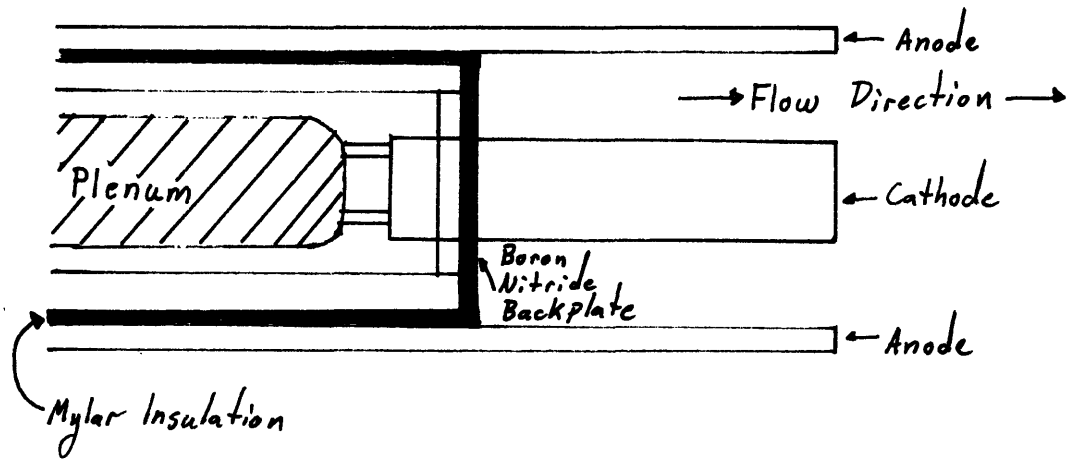

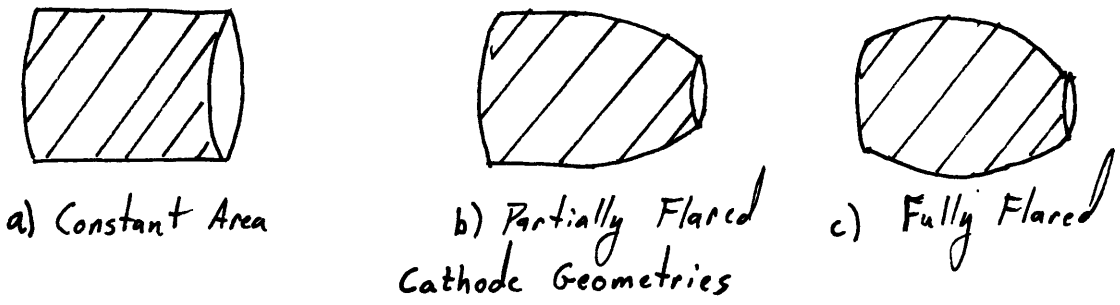

Figure 3.2. Schematic of MPD arcjet with sketches of the three geometries that were investigated. a) Constant area b) Partially flared c) Fully flared.

configuration, the bank provides a current pulse of about 35,000 amps for 800 μseconds. Figure 3.3 shows a schematic of the supply. The additional consideration of matching impedances required a ballast resistor in the network. The current is carried to the MPD on a bundle of coaxial cables where the anode–cathode gap completes the circuit.

One serious concern in this area is the effect of the large transient electromagnetic field present during the current pulse. Special consideration had to be given in order to avoid creating ground loops (electrical paths around which electrons can be made to travel) which could pass current during the transient. To protect the majority of the equipment, a large Faraday copper screen cage was used to house the timing circuitry and data acquisition equipment. A large ground plane (approximately 3 feet high by 30 feet long) was used to keep the screen room potential at the same ground reference as the arcjet. The optical table was completely electrically isolated.

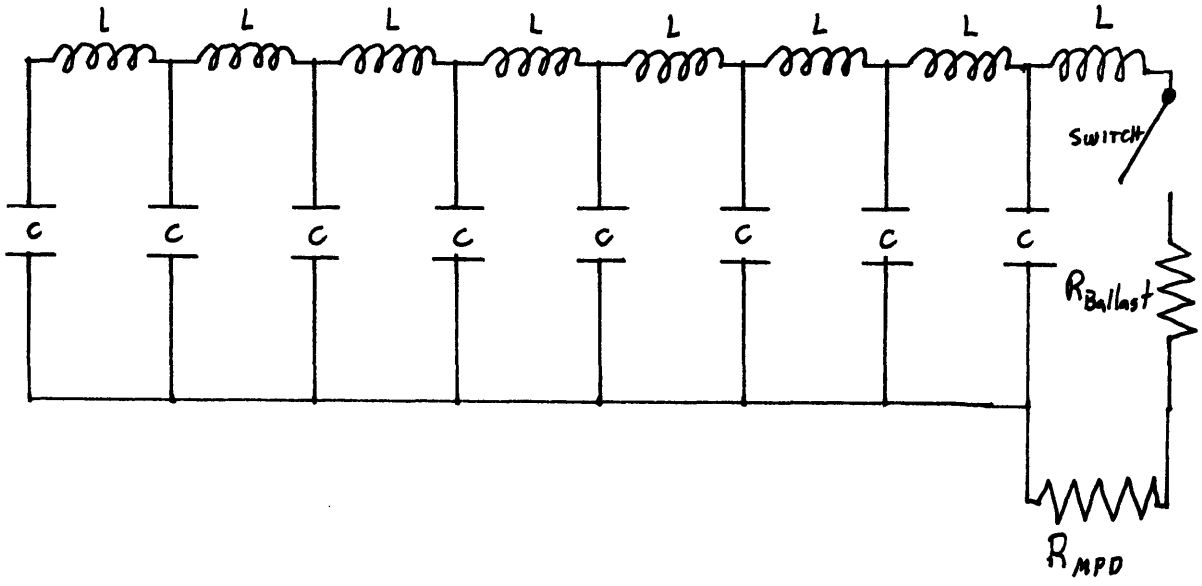

Figure 3.3. Schematic of power supply system as an 8 stage L–C ladder network.

A timing circuit designed by Steve Seiler allowed coordination of all the events necessary for firing. A typical firing sequence would be: Sequence initiation — propellant valve firing — delay — power supply firing — data acquisition trigger.

While this description of the MPD system was brief, the actual design process was quite lengthy. It involved numerous important considerations that were scarcely mentioned here. As the focus of this paper is optical diagnostics, however, a more lengthy discussion is not appropriate. For such a discussion, once again, refer to Daniel Heimerdinger's PhD thesis.

3.3 The Optical System

The proper design of the optical system is crucial to the success and accuracy of the spectral diagnostic methods. The effect of each component in the optical train must be clearly understood if one is to reliably interpret the data. This point is especially directed to the issue of spatial resolution which governed much of the optical design. The simplest way to achieve spatial resolution is to pick out only that light which leaves the source parallel to some reference position. In this case, the observed light represents an integration along the line the light travels upon. In the case of a two–dimensional plasma discharge, picking the line perpendicular to the plasma flow direction and the dimension of flow property variation, this integration involves identical sources within the plasma, as can be seen in figure 3.4a. In the case of an axi–symmetric plasma discharge where plasma properties are soley a function of radius, the integration can be analytically unfolded to yield a radial profile through the Abel inversion. Although the strictly two dimensional case would be simpler to analyze, the axi–symmetric method was used in this investigation. It is appropriate at this point to mention one pitfall. One might think of using a lens to simply "focus" on a spot inside the plasma. While it is true that one can arrange a lens such that light from a small region is made parallel (and therefore

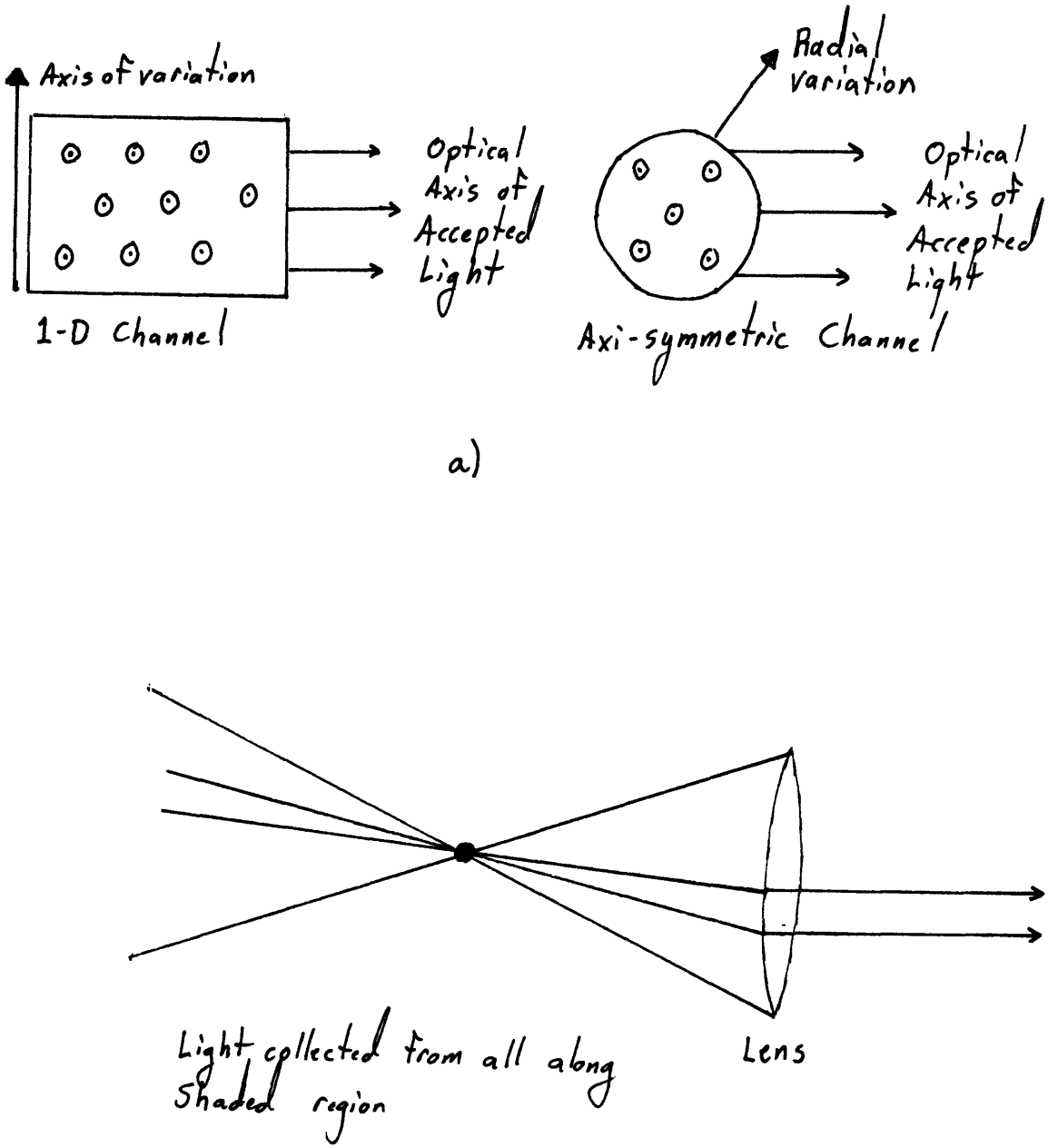

Figure 3.4. A pictorial representation of the spatial resolution capability. a) light collection geometry b) Failure of simple lens with focal point collection.

distinguishable), emissions from the plasma on either side of the focus are also collected in such a way as to make it impossible to spatially distinguish the light from the "focus". Figure 3.4b clarifies this point. Thus, the basis of the optical train is to sort out that light which leaves the discharge parallel to the line of sight. What follows is a discussion of the two subsystems: the optical train and the spectrometer.

Referring to the schematic in figure 3.5, there are nine elements in the optical path for directing and manipulating the plasma emission. A Plexiglass portal lies first in the the train. Plexiglass is considered opaque for wavelengths under 4000 Angstroms. Thus, ultraviolet analysis would require the replacement of the portal with a material such as quartz which has excellent transmission below 4000 Angstroms. The following three elements are three–inch diameter first–surface mirrors to guide the desired light into the

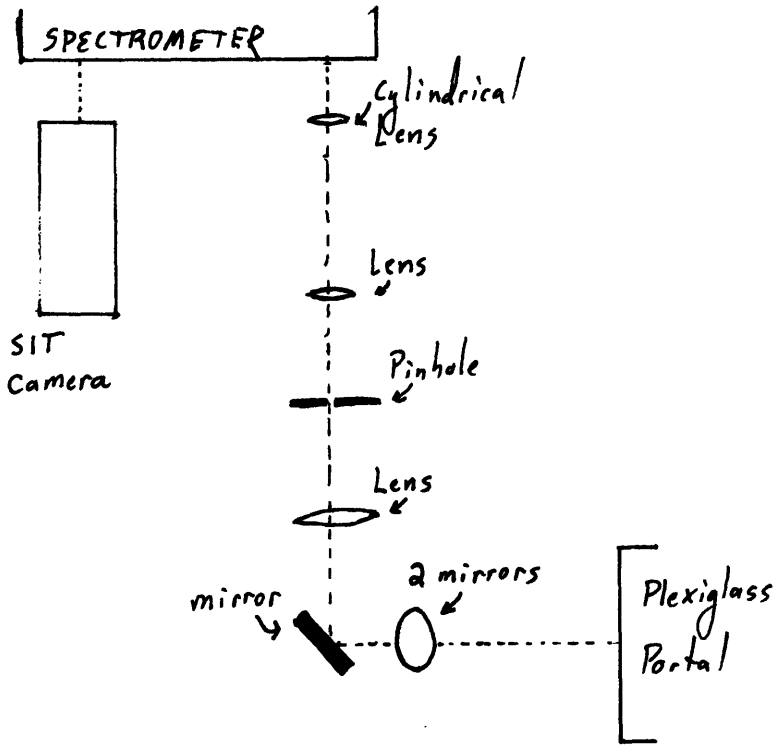

Figure 3.5. Schematic of optical system with nine elements.

optical axis of the spectrometer. At this point, a great deal of the emitted light has been sorted out but as yet no spatial resolution exists. The fourth element is a three–inch ultraviolet grade lens (focal length = 500 millimeters). At the focal point of this lens is a 200 micron pinhole. This pinhole gives the spatial resolution. Light that enters the collector lens parallel to the optical axis is passed through the pinhole while all other light is stopped. The theoretical spatial resolution can be calculated. The ratio of the pinhole diameter, d_p, to the focal length, f_l, is equal to the ratio of the spatial resolution size, δd, to the distance from the lens to the discharge, l_{lp}.

$$\delta d = \frac{d_p}{f_l} l_{lp} \qquad 3.1$$

The theoretical value is 0.6 millimeters for the optical setup used in this study. A second lens recollimates the selected light. This lens is also ultraviolet grade and has a focal length of 250 millimeters. By specifying the ratio of the two focal lengths, one can impose any desired magnification factor. Finally, the collimated light passes through a cylindrical lens whose axis is aligned parallel to the entrance slit of the spectrometer. This element increases the light collection efficiency of the system. The chosen lens was a one–inch diameter, ultraviolet grade cylindrical lens with a focal length of 44 millimeters. Having collected the desired emissions, the next step is to disperse them according to wavelength.

The spectrometer used was a SPEX Industries Model 1269 with a 1.26 meter focal length. The grating has 1200 grooves/millimeter and is blazed at approximately 10,000 Angstroms giving a theoretical resolving power, $\lambda/\Delta\lambda$, of 367,200 in third order. This implies, for instance, a resolution of 0.01 Angstroms at 4000 Angstroms in third order.

3.4 The Data Acquisition System

The heart of these diagnostic methods is a device capable of digitizing and recording the two–dimensional array of information presented by the spectrometer. The Princeton Applied Research Model 1254 silicon intensified multi–channel detector (SIT) along with

the Model 1216 multichannel detector controller serves this purpose. Two computers and a significant amount of software complete the system.

The SIT camera is essentially a plane field of several million photodiodes. The diodes have a common cathode and isolated anodes, which are selectively addressed by a scanning electron beam. As light or photoelectrons fall upon the target, the charge stored in the diode is depleted. When the beam scans the target, a current flows which is proportional to the depleted charge. This current is integrated by a preamplifier to convert the signal back to total charge. The electron beam also serves to recharge the photodiodes. Positioned in front of the silicon target is an intensifier section consisting of a fiberoptic facial plane that channels incident photons onto a photocathode. The photoelectrons subsequently emitted are accelerated by up to a nine kilovolt potential before striking the silicon target. This is the mechanism whereby the two–dimensional array of spectrographic data is digitized.

One drawback of the SIT camera is the effect of a phenomenon called dark current. Each diode cannot indefinitely hold its charge. Thermal effects allow the charge separation sustained by the diode to equilibrate. The dark current effect is a function of temperature and can be dramatically reduced with a moderate amount of cooling. For the signal levels involved in this experiment, however, there were no noticeable dark current effects. Thus, cooling was not necessary.

The intensifier section of the SIT camera allows for extremely rapid "shuttering." The multiplying effect relies on a high voltage being applied to the photoelectron. By lowering this voltage, the intensifier can be essentially turned off and prevent any light from falling on the target. This gating ability was used for time exposures as small as 100 μseconds. Potentially, the exposure time can go as low as 100 nanoseconds.

An IBM System 9000 computer and software written by Kevin Rhoads of the M.I.T. High Voltage Research Laboratory was used to program the controller and record digitized images. A number of analysis and plotting options were also available with this

software. To facilitate the more complex analysis involved in extracting radial plasma properties, the data was subsequently transferred to an IBM AT system. A commercially available computing package called ASYSTANT$_{tm}$ was then used to complete the analysis.

The data acquisition system is admittedly cumbersome. The use of multichannel detector systems is, however, a relatively recent event and it is difficult to find a completely integrated system suitable for advanced spectrographic analysis. For example, data input/output standards of the Model 1216 controller differ slightly from those used by IBM in their System 9000. It was therefore necessary to construct an electronic interface circuit to overcome this. The circuit, designed by Kevin Rhoads, is shown in Appendix 2.

3.5 Procedures

The experimental procedure for obtaining the data was straightforward. A suitable wavelength for each diagnostic technique was chosen and the spectrometer was tuned to it. The data acquisition system was triggered at the appropriate time by the master timing circuitry. When time resolved data was required, the gating device was also triggered by the timer. Immediately following the MPD firing, the data was evaluated and, if appropriate, stored. Chapter 4 discusses the data and plasma properties indicated by them. Four preliminary procedures were, however, required in order to perform the subsequent analysis accurately.

3.5.1 Optical Focus

Accurate interpretation of a line profile relies on accurate knowledge of the system resolution in wavelength. The highest obtainable resolution is, in theory, fixed by the spectrometer. As noted before, this value is about 0.01 Angstroms. In the arrangement used in this experiment, the SIT camera face was coincident with the spectrometer exit plane. The SIT camera target has a physical resolution of 500 by 512 pixels (a pixel being the smallest bundle of photodiodes addressable by the electron beam). Physically, each pixel is

about 0.024 millimeters wide. In first order, the spectral dispersion at 5000 Angstroms (Å) is 6.47 Angstroms/millimeter. Combining these numbers, the SIT resolution is about 0.16 Å. It is important to note that the resolution is proportional to the dispersion, i.e. in third order resolution rises to 0.05 Angstromss. The theoretical resolution could be reached with the addition of an optical system to increase the spectral dispersion so as to match spectrometer and SIT resolutions. Such a device is described in Appendix 3. To experimentally confirm how the actual focus approaches these ideals, a mercury spectrum lamp was used. The linewidth of this cool discharge should be vanishingly small. Thus, any observed broadening should be due to the optical focus. Figure 3.6 shows a typical mercury profile. Repeated adjustments of the SIT camera position yielded a resolution of approximately two pixels, or 0.33 Angstroms, in first order. The resolution was defined as the full width at half maximum of the the mercury 4358 Angstroms line. The difference between actual and theoretical focus is attributed to side channel cross talk in the detector, where adjacent pixels are affected by the charge of their neighbors, and the focusing of the internal intensifier section.

3.5.2 SIT Camera Response Calibration

If a completely uniform light source (in both wavelength and space) was placed at the start of the optical train, the image recorded by the SIT camera would not be uniform. A variety of factors cause this variation. A circular lens collects an amount of parallel light that varies along the vertical axis. This is simply because the lens width is equal to its diameter at the center and falls off to zero at the top of the lens. Another variation is introduced by any misalignment of the cylindrical lens with respect to the spectrometer slit axis. In fact, misalignment of any component can generate artificial signal variations. Finally, the SIT camera can have a varying response across its face. All of these factors can be accounted for by a experimentally determined response function. This correction can be found by imaging a known uniform source on the SIT face and designating the recorded

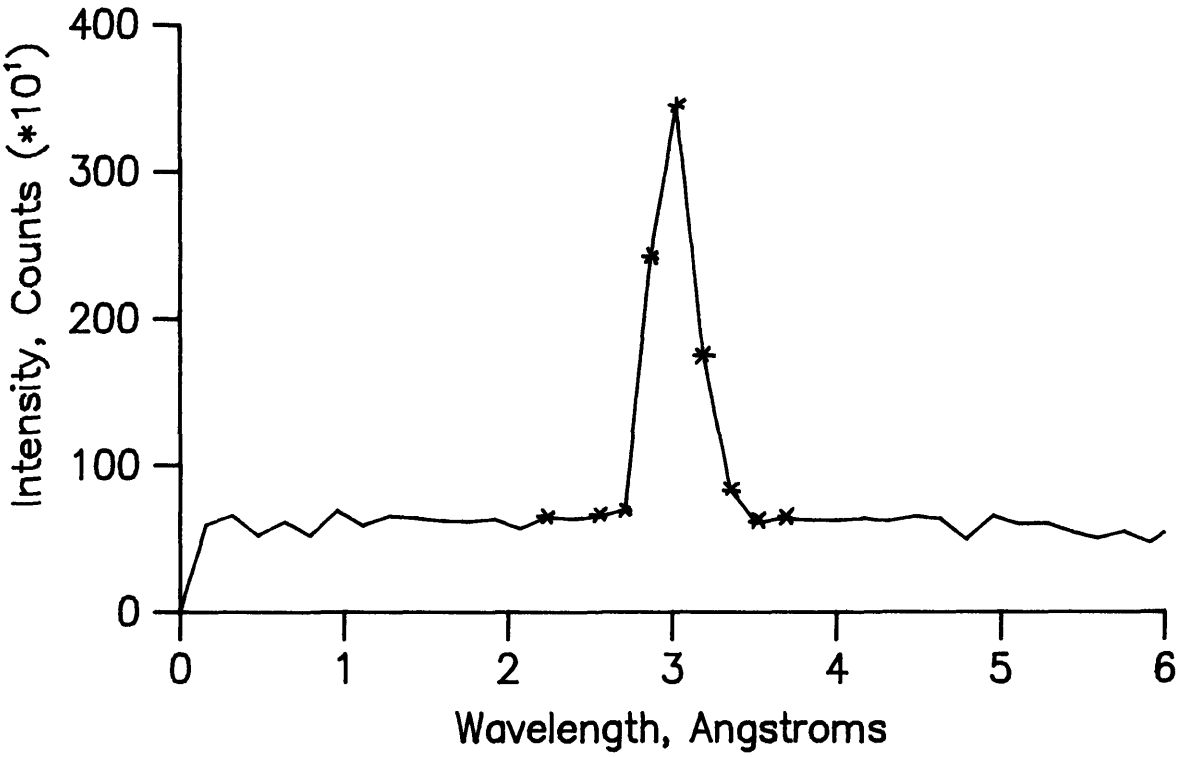

Figure 3.6. Typical profile of mercury line used to establish best focus.

image as the response function. Such a calibration was performed and the results are given in the next chapter.

A linear response to incident intensity is clearly required. Although the SIT camera specifications claim a dynamic range of 1 to 16383, the linear range may be substantially less. To check this, a helium neon laser and a series of neutral density filters were used to bring various levels of intensity to the SIT camera. The relative response would then indicate the linear regime. Again, these results are reported in chapter 4.

3.5.3 Wavelength Calibration

The relative intensity calculation requires the comparison of lines that may differ markedly in wavelength. A calibration of the system with respect to wavelength is therefore necessary. The calibration source was an Optronic Laboratories Model 550C

tungsten ribbon–filament lamp. The lamp was operated at 15 amperes (± 0.01 amperes) DC for which tables of spectral radiance were provided. The uncertainty in current contributed less than an 0.5% error in the spectral radiance. Images were recorded at various wavelengths and filters were used to keep out higher orders of light. The resultant intensity levels at each wavelength were normalized by filter transmission coefficients and the known emission coefficient to yield the relative wavelength response function of the SIT/optical system. Chapter 4 presents these results.

3.5.4 Spatial Resolution Check

As noted before, spatial resolution is crucial to thse diagnostic methods. To quantify this number, a simple procedure was devised. A mercury lamp was positioned at the start of the optical train. An image was recorded. Half of the lamp was now obstructed and another image was recorded. The second image clearly showed a sharp cutoff where the mask had been placed. The spatial resolution was then defined to be the distance from full intensity to half intensity at the cutoff.

Chapter 4

Results and Discussion

4.1 Introduction

Interpretation of the spectroscopic data proved to be complicated. The MPD thruster was found to operate in a regime that did not permit straightforward application of the classical optical techniques. The ionization fraction of both argon and hydrogen was close to unity. Thus, neutral argon, useful for an accurate electron temperature measurement, was absent. Furthermore, the hydrogen mostly became protons making it virtually impossible to detect any but the brightest hydrogen line. The electron density was found to be on the order of 10^{-15} cm^{-3}. As noted in chapter two, the application of a local thermodynamic equilibrium model becomes problematical at this level. This low density even posed problems for methods not based on LTE as the Stark broadening lowered to the order of Doppler broadening and instrumental width. Nevertheless, estimates could be made of electron density, electron temperature, and ion temperature. In addition, the data acquisition system was fully characterized.

4.2 Data Acquisition System Characterization

The optical multichannel analyzer system was tested using standard light sources to determine its operating characteristics.

An absolute and relative intensity calibration over wavelength was performed with a tungsten filament ribbon lamp. By placing the lamp in the plane of the MPD discharge axis and accounting for the transmittance of the neutral density and bandpass filters placed in the optical train, a transfer function was arrived at to relate the data system intensity units to the spectral radiance of the source in watts per square meter per steradian. The factory calibration provided with the lamp was used to arrive at this transfer function.

Figure 4.1 gives the optical transfer function over wavelength. Two features are worth noting. The system has a rapidly varying response around 6000 angstroms. Most ionized argon lines are below 5000 angstroms so this posed no problem. Future work with neutral argon, however, may be impeded by this behavior. Secondly, below 3700 angstroms, the response drops dramatically. This has implications for any attempt to look at ultraviolet lines as will be noted later. Apart from these points, the profile is typical of such photomultiplier based systems.

The response of the detector over illuminating intensity was also determined. Figure 4.2 shows the response of the SIT camera to increasing intensity. There is one important result. Although the dynamic range of the system is 1 to 16383 counts, the response is

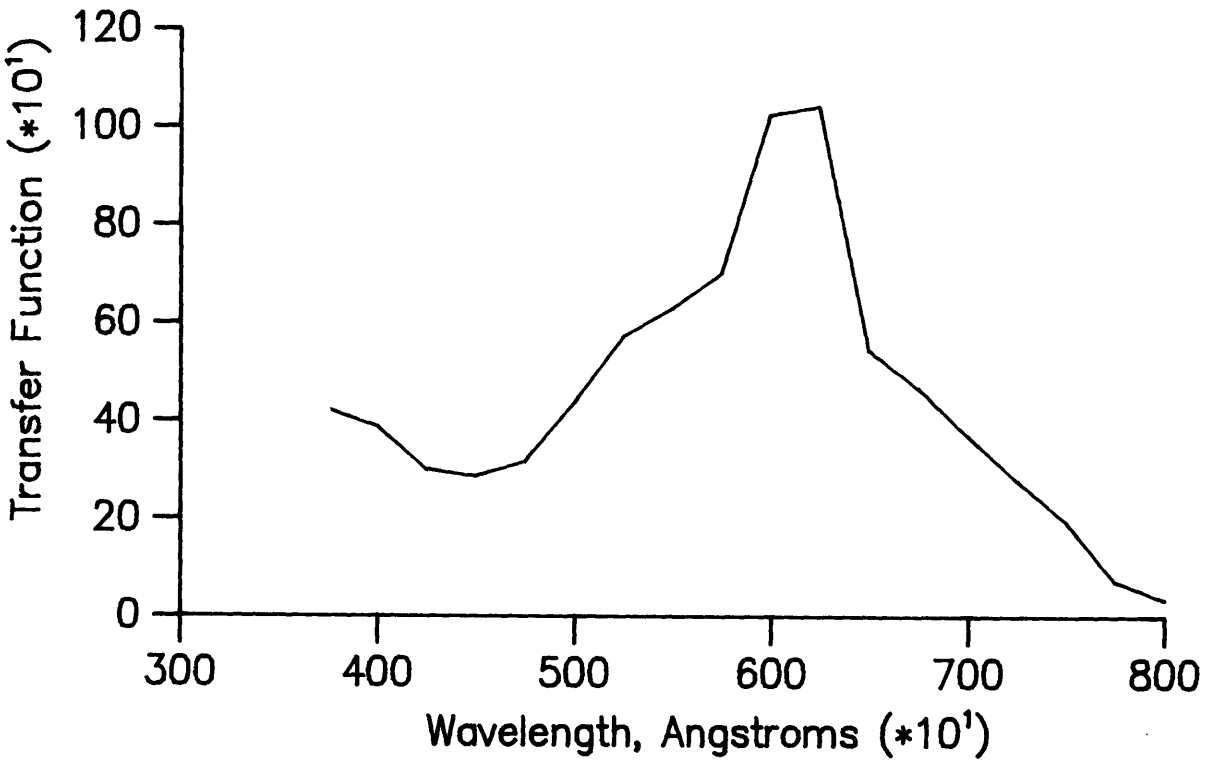

Figure 4.1. Absolute intensity calibration of SIT camera relating counts to spectral radiance of source.

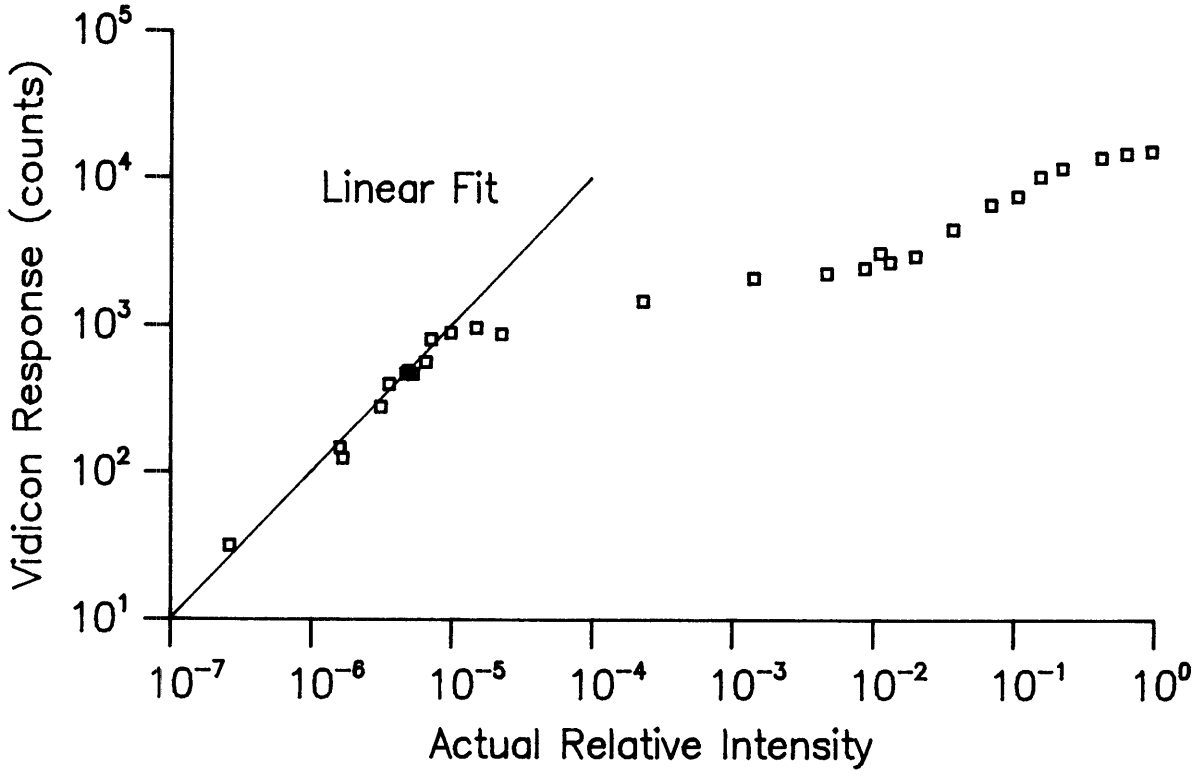

Figure 4.2. Response of SIT camera to increasing intensity.

linear only up to approximately 900 counts. Care was taken to keep all signal levels below this threshold.

The spatial resolution of the acquisition system was determined in a simple manner. A mercury spectrum lamp (consisting of a long thin tube) was positioned at the start of the optical train. A mask allowing one centimeter of tube length to emit into the optics was then placed on the spectrum lamp. Ideally, the image on the SIT camera should have a sharp edge. In practice, the number of pixels between full intensity and half intensity was designated at the spatial resolution. This was found to be about 8 pixels. Knowing that the image represented one centimeter of source, a spatial calibration could be determined. This was found to be about 0.15 mm/pixel. The cathode separations were between 2 and 4

centimeters, so this resolution allowed 40 to 80 data points across the channel in the typical operating mode where four pixels comprised a single point.

The camera did have a marked "pincushioning" distortion. The distortion is a result of the camera's internal focus lying on a curved surface rather than a planar one. This results in a defocusing of images near the edge of the screen and an artificial curvature being imposed on the normally straight spectral lines. For the spectral line integration methods this had no effect. For line profile measurements, care was taken to keep the line in the central undistorted region of the camera. Figure 4.3 shows a typical spectra of argon lines where this curvature is evident.

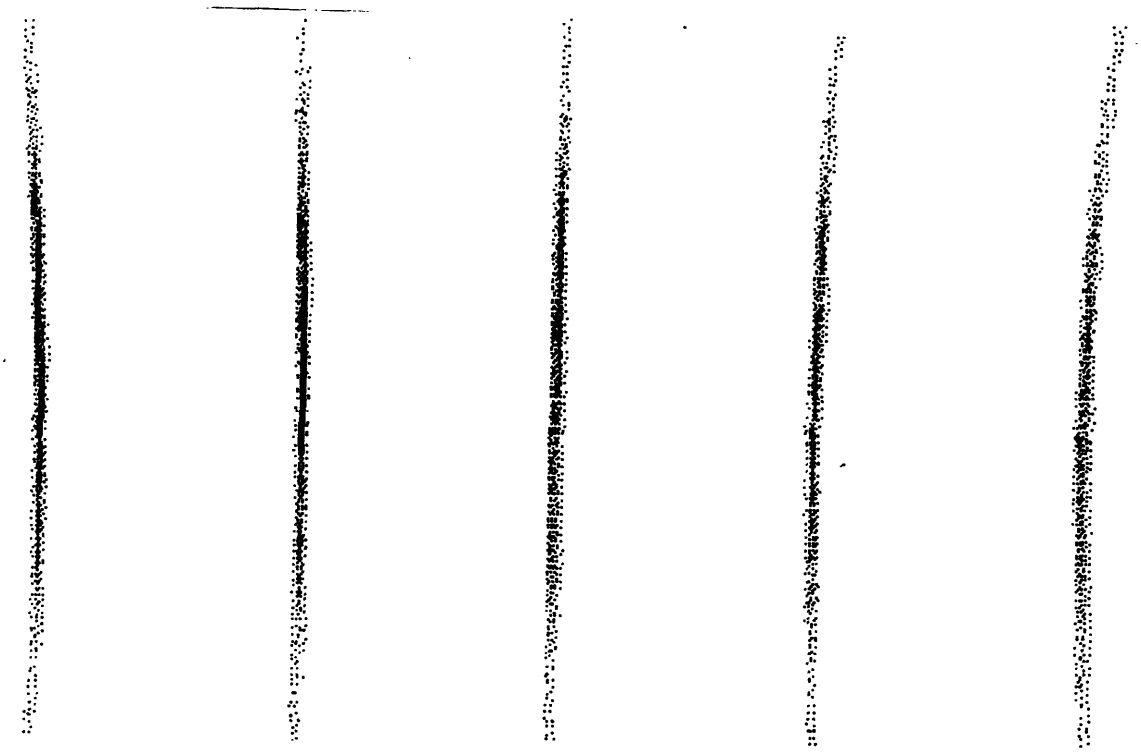

Figure 4.3. Example of spectra exhibiting "pincushioning" behavior.

Finally, there were no optics between the spectrometer exit plane and the SIT camera face. In fact, the camera was mounted flush to the spectrometer. This configuration fixed the spectral dispersion to 0.16 angstroms/pixel in first order, a number nearly three times larger than the actual resolution of the spectrometer. Future work interested in more detailed profile measurements could make use of some additional optics to lower the resolution to the theoretical value of 0.06 angstroms at 5700 angstroms in first order. Appendix three describes the design of such an auxiliary system.

4.3 Electron Temperature Measurement

Electron temperature was by far the most comprehensive measurement taken in this study. Data integrated over the entire discharge time, data extracted only from the equilibrium time, as well as data taken from before and after the initiation of the the voltage fluctuations associated with onset were all used to compute electron temperature, T_e. Two similar techniques were used to extract T_e from the measured intensity. One was the classical relative line intensity method based on intensity ratios. The variation on this of simply plotting the logarithm of the intensity (corrected by the appropriate atomic constants) versus upper energy level gave generally agreeable values for T_e however it was also useful in investigating the expected LTE assumption breakdown at lower energy levels as will be discussed in the next few pages. The measurements also suggested certain conclusions about transient effects and plasma behavior after onset initiation.

Time integrated data for the MPD thrusters was taken during two experimental runs. In the first run, the constant area channel was operated at 13 kilovolts bank charge with a plenum pressure of 470 torr giving a mass flow rate of about 4 grams/second. Three spectral lines were recorded of ionized argon (ArII): 4103.91 Å, 4621.3 Å, and 4609.6 Å. The atomic constants for these lines and all other lines used in this study are tabulated in Appendix 4. All three pictures were taken with a 100 micron spectrometer entrance slit

width and in first order. The operating mode for the SIT camera for this data and most other T_e data was with the pixels grouped into a 128 by 250 array. Figure 4.4a gives the radial intensity profile for the 4103.91 Å ArII line. The dashed line represents the noise–filtered result while the solid line is the actual data. In this case, and most others, a series of pictures were summed together to enhance the signal to noise ratio. Three frames of data were summed for this line. Figure 4.4b shows the Abel inversion of the data. The radial distribution of T_e was then computed using the relative line intensity method. The correlation coefficient of the line fit to this data was approximately 0.96 where 1.0 is a perfect fit. The result (in electron volts, eV) is given in figure 4.5 along with those for the other channels. In the constant area channel, the electron temperature remained essentially constant between the electrodes at 2.0 eV. The uncertainty in electron temperature is estimated to be ±40%. For the partially flared channel at the same operating conditions, three ArII lines were used: 4448.88 Å, 4609.6 Å, and 4103.91 Å. Examination of figure 4.5 reveals a generally lower electron temperature than in the constant area case. This suggests less dissipation of power into plasma heating. The theory developed by Martinez–Sanchez and Heimerdinger predicts that channel flaring would increase performance and lower dissipation. Whether the decreased dissipation is attributable to a more uniform electric field or simply fluid dynamic expansion is an issue beyond the scope of this work. The correlation coefficient varied from around 0.8 near the cathode to 1.0 at the anode. Figure 4.6a shows a Boltzmann plot near the cathode and figure 4.6b shows one near the anode. Clearly, the data near the cathode is unreliable either because of error or an LTE breakdown. This feature disappeared in the second run of experiments suggesting that some error was responsible for this discrepancy. The uncertainty is estimated to be ±36% near the anode. Finally, the fully flared channel was diagnosed at the same operating condition using three ArII lines: 4226.99 Å, 4103.91 Å, and 4609.6 Å. Once again, electron temperatures were generally lower than those in the constant area channel (see figure 4.5) further supporting the lower dissipation expectation. Also, the data near the cathode was

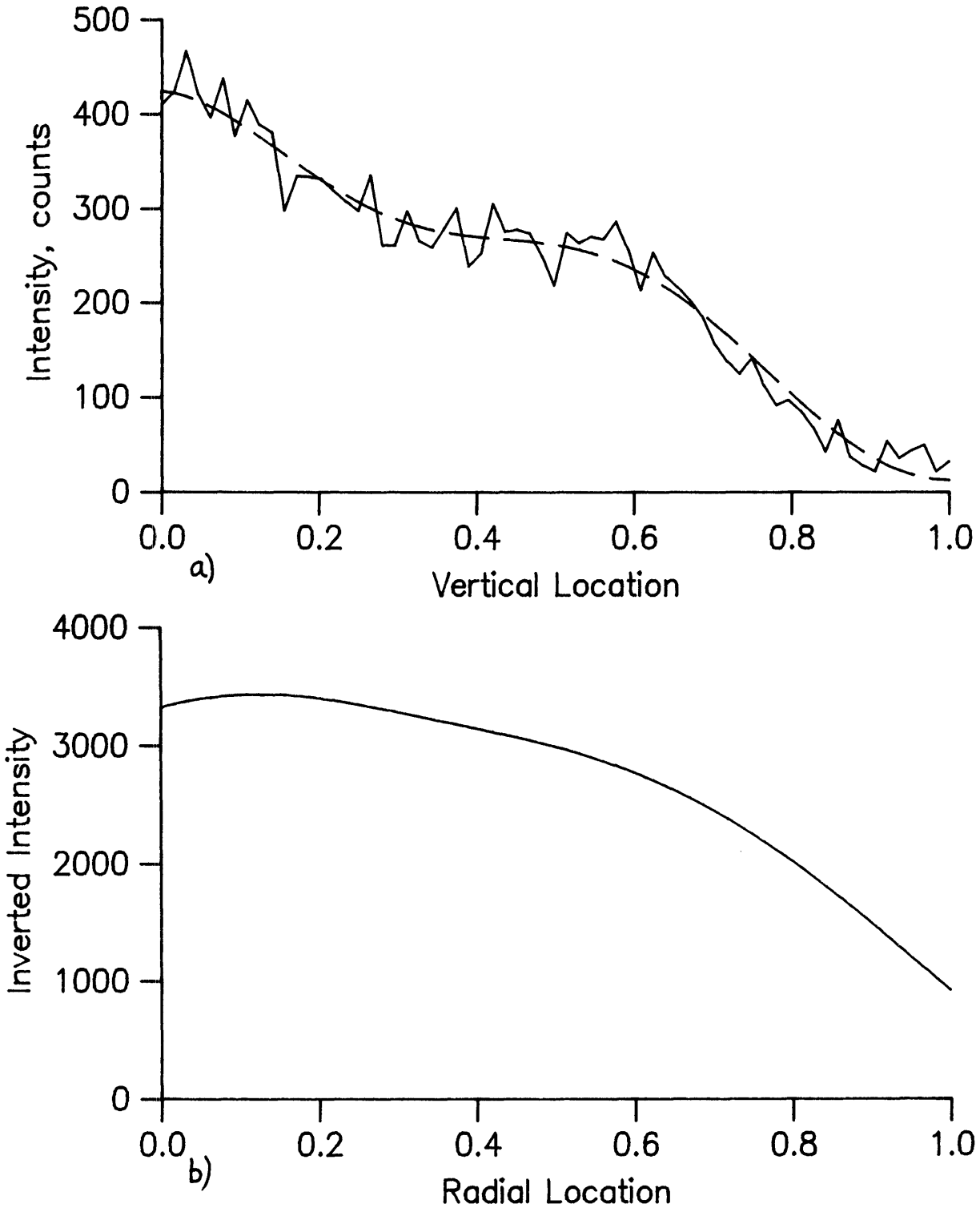

Figure 4.4. Sample electron temperature data reduction. a) Raw intensity data for 4103.91 Å line b) Abel inversion result.

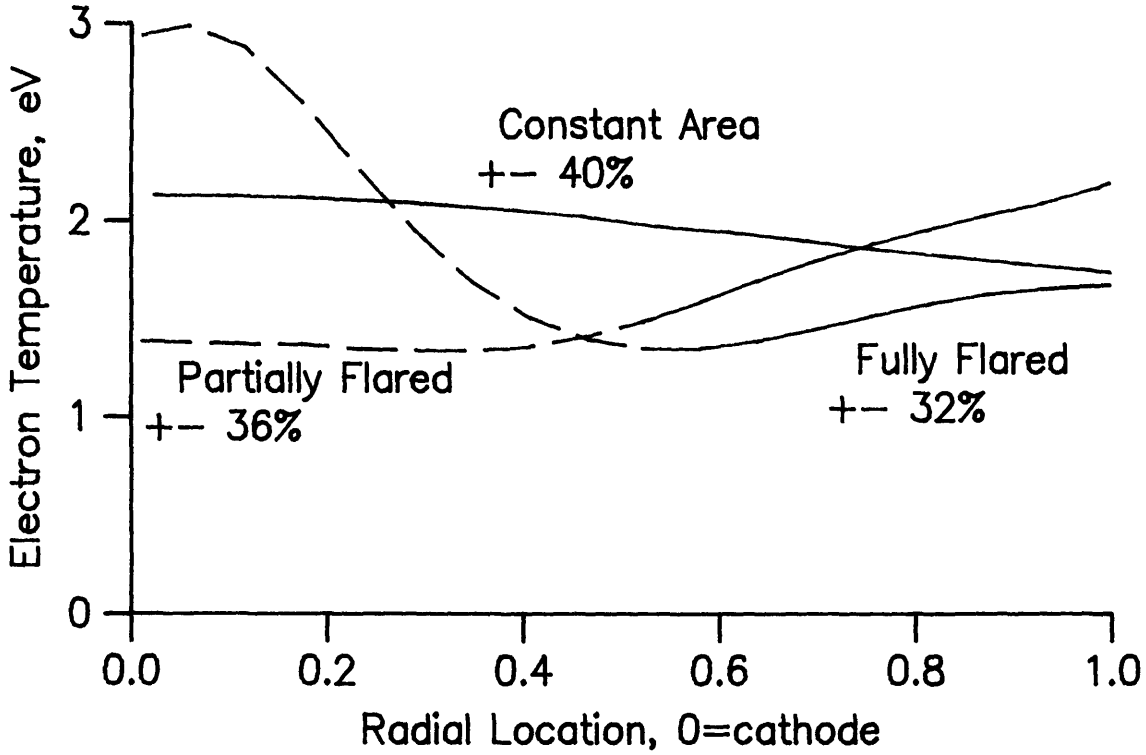

Figure 4.5. Electron temperature results for the first run of experiments. The dotted lines indicate unreliable data.

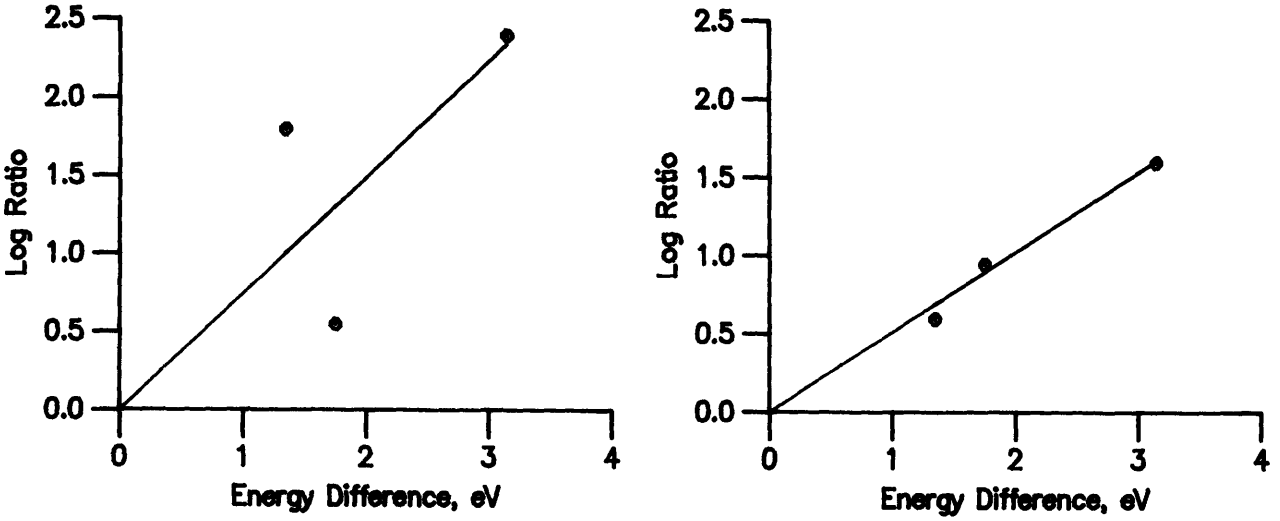

Figure 4.6. Examples of Boltzmann plots for T_e determination in partially flared channel. a) Near the cathode b) Near the anode.

not believable as the correlation coefficient was as low as 0.6. For the outer two–thirds of the channel, however, the data was very linear giving excellent correlation coefficients. The uncertainty is estimated to be ±32%. All three measurements were only based on three lines and hence the uncertainties in actual values are rather large. Nevertheless, the trend of lower dissipation with flaring is strongly suggested by the results from the first experimental run.

The second experimental run was substantially more comprehensive than the first. Unfortunately, time only permitted analysis of one channel, the fully flared configuration. The time integrated data for this run consisted of six ArII lines: 4079.6 Å, 4042.9 Å, 4072.01 Å, 4103.91 Å, 3737.9 Å, and 3729.16 Å. The greater number of lines permits substantially more confidence in the line fit to yield T_e. The operating condition was again 4 grams/second but the charging voltage on the bank was 11 kilovolt (just below the value that initiates onset hash). The data consisted of six summed shots. Figure 4.7 gives the radial distribution of electron temperature (along with the distributions for the two other operating conditions). The magnitude agrees well with the data from the previous run. Once again the data is more linear in a plane of log(intensity) versus energy near the anode than near the cathode but only marginally so. There is no reason to doubt the validity of the cathode data in this measurement. The uncertainty in these values is ±18%.

The next data set used the gating capability of the SIT camera to collect only light emitted between 150 and 400 microseconds into the discharge. The lower overall intensities only permitted three lines to be accurately measured: 4072.01 Å, 4103.91 Å, and 3729.6 Å. The linearity of the data, though, was good with an average correlation coefficient of 0.96 and an uncertainty of ±25%. The result has the same trend as the time integrated case and differs little in magnitude (see figure 4.7). The implication is clear. The start–up transient has little effect on an electron temperature measurement. In other words, the transient is a primarily a density effect and not a temperature effect. This result will make future T_e measurements substantially easier to make.

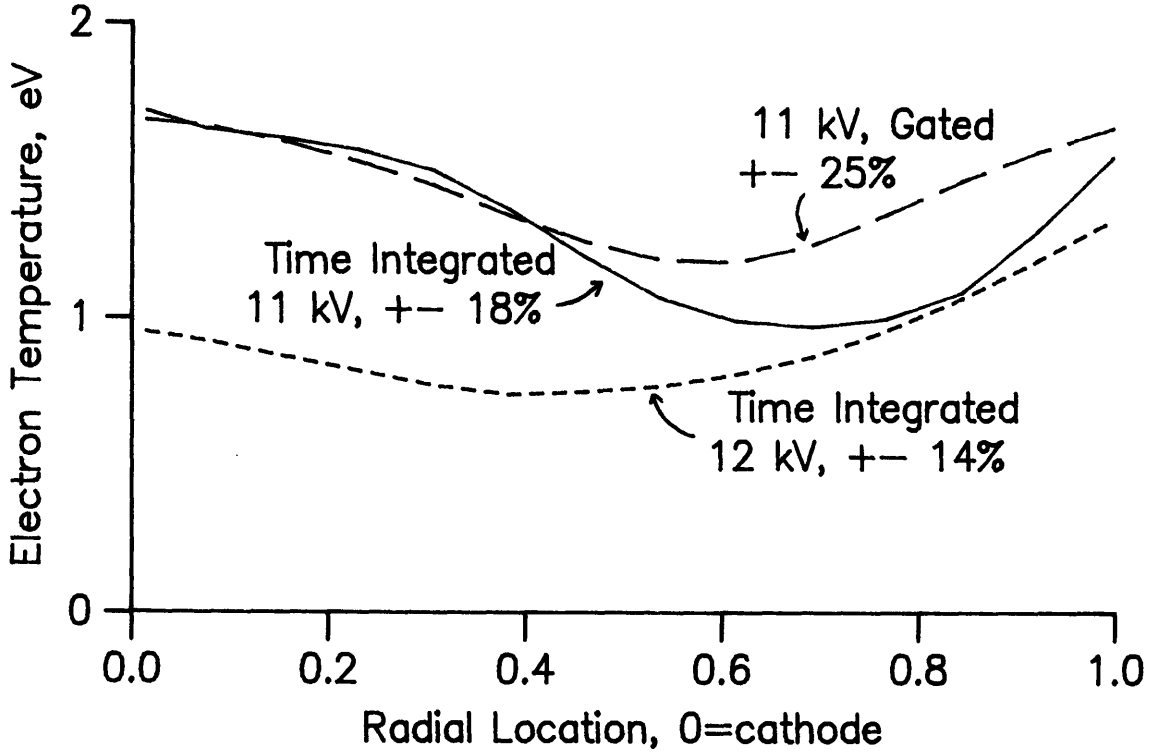

Figure 4.7. Electron temperature results from the second run of experiments.

Finally, an electron temperature measurement was made at a charging voltage of 12 kilovolts (where interelectrode voltage fluctuations were present). Figure 4.7 shows a nearly 50% reduction in temperature near the cathode while anode temperatures remained virtually unchanged. This data was based on four ArII lines: 4042.9 Å, 4072.01 Å, 4103.91 Å, and 3729.3 Å. Once again, the linearity of results was good (uncertainty was ±14%). Examples of Boltzmann plots for these measurements are given in figure 4.8. The data point at the lowest energy level in the figure was not used for this measurement.

The lowering of T_e near the cathode is so substantial that it is difficult to just attribute it to error. In fact, the intensity of the 6328 Å line of hydrogen was seen to increase notably in going from 11 kilovolts to 12 kilovolts. This indicates a lower ionization fraction for the plasma and, hence, a lower temperature. No reasoning was conceived for

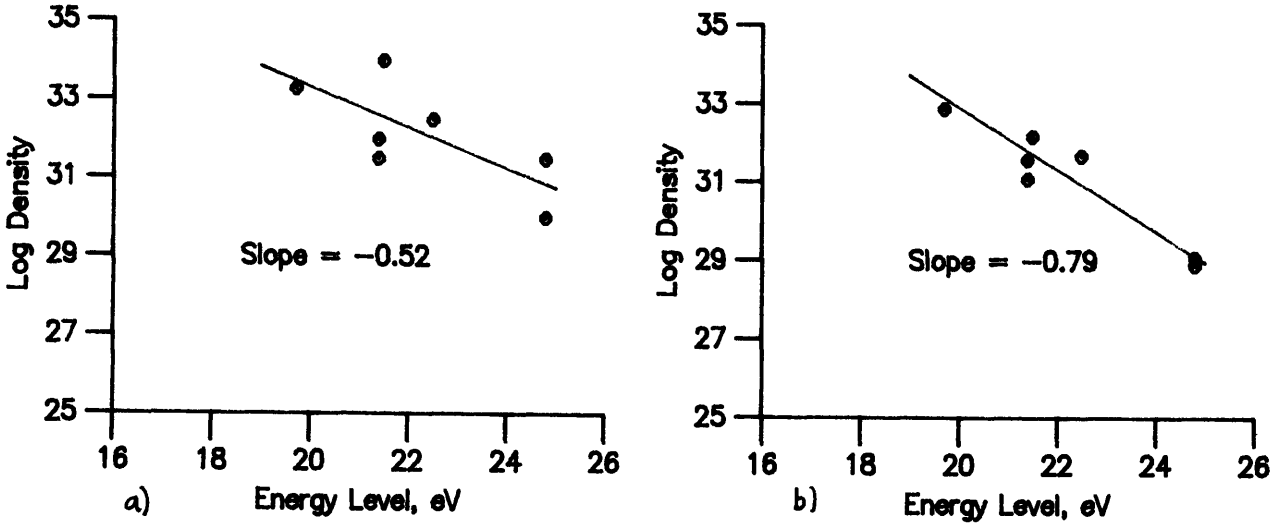

Figure 4.8 Sample Boltzmann plots from the time integrated, 11 kV condition in the fully flared channel. a) Near the cathode b) Near the anode.

explaining a cooler cathode but not a cooler anode. The anode data may be actually lower than shown because of the uncertainty. Perhaps this is the case as a plasma with an overall lower electron temperature is more believable. More work is needed to explain this phenomenon.

A second method was used to calculate electron temperature that represents a variation on the relative line intensity method. As noted in chapter two, equation 2.11a, the ratio of intensity to gf/λ^3 is proportional to the population of the upper excited level. Thus, a plot of the logarithm of this ratio versus upper level excitation energy should yield a line whose slope is $-1/T_e$. This was done (figure 4.8 is an example) and the results matched the earlier ones to within 5% in most cases and 15% in all cases. By not taking

ratios of intensities one can obtain a clearer picture of the actual population distribution in the upper levels.

A final result to report concerns the validity of the LTE assumption discussed in chapter 2. The simple models used suggested a threshold of about 5–6 eV below the ionization potential of ArII, 27.6 eV. Data were taken from the 4082.04 Å line of ArII that lies about 8 eV below the ionization limit. Referring to equation 2.11a, the ratio of intensity to gf/λ^3 is proportional to the population in the upper excited level. If LTE were completely valid, a plot of the logarithm of this ratio versus the level energy should yield a straight line. Figure 4.8 shows such plots for the 11 kilovolt time integrated data set. The lower energy population is not noticeably lower than what is predicted by purely LTE considerations (an extrapolation of the line fit to the upper levels). It is important to recall, however, that the logarithm can make large discrepancies appear small. The model presented in chapter 2 appears to yield a conservative estimate of the threshold. In fact, an LTE assumption appears valid at least 8 eV under the ionization limit. Clearly a more exhaustive examination of line intensities is necessary to confirm this.

4.4 Electron Density Measurement

The electron density measurement was not nearly as definitive as the electron temperature measurements. A clear conclusion that surfaced immediately, however, was that the plasma was nearly fully ionized. Neutral argon lines could not be found in the spectra. The electron temperature supports this conclusion. The classical Saha equation for ionization fraction is[33]:

$$\frac{\alpha^2}{1-\alpha} = \frac{3.0 \times 10^{27}}{n_t} T_e^{1.5} \exp(-X_i/T_e) \qquad 4.1$$

Where α = ionization fraction
n_t = total number density [m^{-3}]
X_i = ionization potential [eV]

For the temperatures indicated earlier and a density of 10^{16} cm^{-3}, the ionization fraction is 0.94. If the density is lower (as it most likely is), this fraction will be even higher yet. Of course, this expression only presents an upper bound as the plasma is not likely to be in Saha equilibrium because of the numerous recombination processes present. The advantage of a high ionization fraction is that the electron density can essentially be set equal to the heavy particle density. The disadvantage is that the hydrogen in the plasma becomes mostly protons. The Stark broadening technique, based on the width of hydrogen lines, becomes difficult to use with such low densities, and hence, low intensities. Nevertheless, some sense of the density can be obtained.

As a check on the Stark broadening technique, a measurement was made on the dense plasma jet being investigate at R&D Associates. The device is somewhat similar to the MPD arcjets. It operates at a lower mass flow rate, ~ 2 grams/second but the device itself is much smaller and densities were nearly an order of magnitude higher. Figure 4.9 shows a typical profile of the Hα line from the jet. The solid line is the lorentzian profile fit to the data. The agreement could well be called amazing. Using the theoretical relationship between Hα full width at half maximum and electron density, the radial distribution of n_e was calculated to an accuracy of better than 10%. The theoretical relationship is shown pictorially in 2.7. The data comes from Hill[34]. A line fit to this gives the following useful equation for Hα:

$$n_e = \exp(1.322 * \ln(\lambda_{1/2}) + 36.29) \quad [cm^{-3}] \tag{4.2}$$

The high ionization fraction and general absence of hydrogen lines despite the use of a 98% Ar/2% H mixture limited the Stark broadening technique to the fully flared channel where electron temperatures were low enough to permit appreciable amounts of hydrogen to remain unionized. Hα was not detectable in either of the other channels to any reasonable degree. Figure 4.10 shows typical data with the associated lorentzian fit at two radial locations. The operating condition was 13 kilovolts with an Ar/H mixture at 470 torr in the plenum giving a mass flow of 4 grams/second. The spectral line was imaged on a

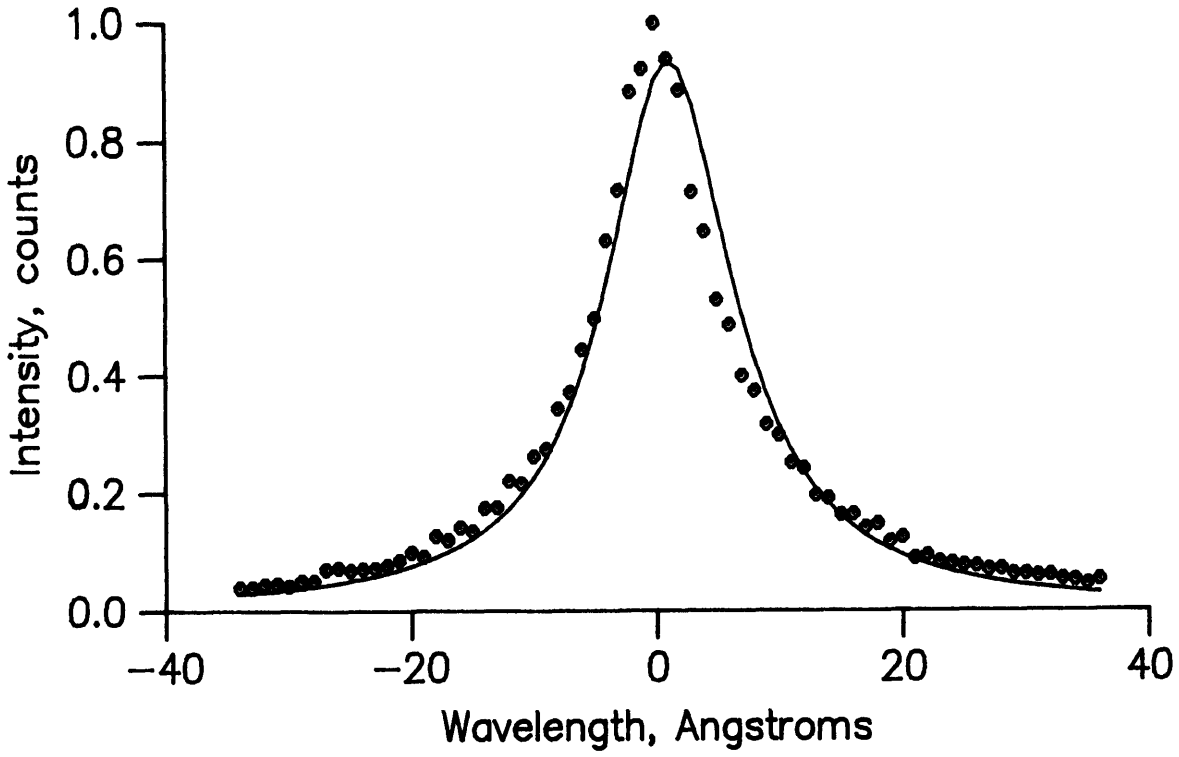

Figure 4.9 Hα profile from the dense plasma jet with the Lorentzian fit superimposed.

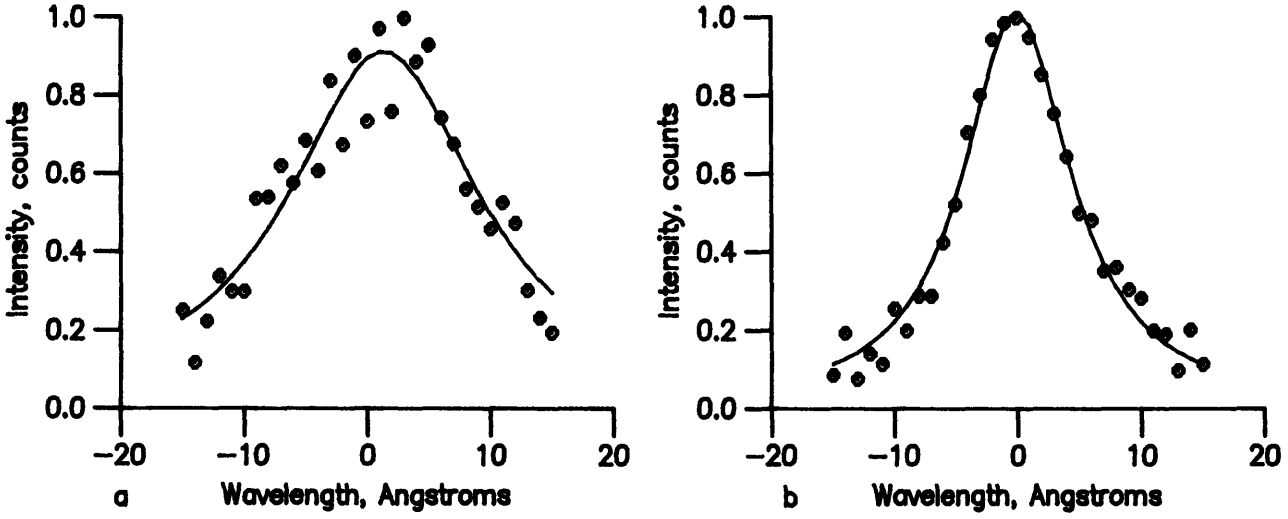

Figure 4.10. Hα profile from the fully flared channel with Lorentzian fit superimposed.
a) Near the anode b) Near the anode

128 x 500 SIT pixel array in second order giving a resolution (instrumental bandwidth) of 0.16 Å and six frames were summed together to improve the signal to noise ratio. Interpretation of this line width was ambiguous due to the presence of both Stark broadening and Doppler broadening. If one is willing to assume that the ion temperature is some constant fraction of the electron temperature, then one can deconvolve the Hα profile using the tabulated Voight profile[35]. A polynomial fit to the Voight profile gave the following relationship between the lorentzian half–width and the doppler half–width.

$$\frac{\lambda_l}{\lambda_t} = 1.00 - 9.031\text{x}10^{-2}\,\frac{\lambda_d}{\lambda_t} - 0.9188\left\{\frac{\lambda_d}{\lambda_t}\right\}^2 \qquad 4.3$$

Where λ_l = lorentzian half width
λ_d = doppler half width
λ_t = total half width

Figure 4.11 gives the results of this calculation for a variety of assumed values for the ratio of ion temperature to electron temperature. The uncertainty in the measured intensity is ±25% and the uncertainty in the smoothed and inverted Hα profile is ±15%. Thus, the uncertainties in electron densities using this technique are estimated to be ±25%. This uncertainty does not reflect the uncertainty as to which broadening mechanism is present. It is purely the numerical uncertainty if the line were completely Stark broadened. For the range of ion temperatures between 0.3 and 4 eV, the electron density remains on the order of 10^{15} cm^{-3} throughout most of the channel. Near the anode, the ion temperature cannot be more than about 1.0 eV for the electron density to be non–zero. Assuming that the ion temperature remains in the 0.3 to 4.0 eV range and spatial gradients in temperature are not severe, one can conclude that there is a substantial decrease in density near the anode. Recalling that this data is taken under onset conditions, this drop may be explained by an anode starvation mechanism such as described by Rudolph, Jahn, Clark, and Jaskowsky[36].

Another interpretation of the profile can yield an average velocity for the MPD.

Defining the average velocity as the mass flow divided by the area integration of density, one arrives at the following relation.

$$4.4 \qquad V_{avg} = \dot{m} \Big/ \int_{r_{min}}^{r_{max}} M_a n_e \, 2\pi r \, dr$$

Where V_{avg} = average velocity [m/sec]
$\dot{m}$ = mass flow [kg/sec]
M_a = atomic mass [kg]
r = radial location [m]

Again, this can be calculated for a range of assumed values of T_i/T_e. Figure 4.12 shows this. MPD's have been shown to typically operate at specific impulses of around 1000 seconds and up. For this device to operate similarly, one is forced to assume an ion temperature of at least 3.5 eV. Unfortunately, this creates a dilema. Either one assumes a specific impulse nearly an order of magnitude too low or one assumes that the ion temperature is substantially elevated above the electron temperature. For the specific impulse to be low, a substantial loss mechanism such as viscosity must play a part. Calculations by Heimerdinger[37] for this channel conclude that viscosity does not contribute significantly to losses. Turning to the issue of ion temperature, two mechanisms can be envisaged that would preferentially pump energy into the ions. Viscous interaction with the electrodes is one such mechanism. Viscosity, however, was already found to be a minor player. A shock is the second mechanism. Clearly, shocks in a nonequilibrium plasma are a complex issue beyond the scope of this work. A simple calculation, however, can demonstrate that such a shock could very easily exist. Heimerdinger, among others, describes the pumping force between the electrodes that tends to "push" the flow towards the cathode. If the flow has a velocity of 10000 m/s and is at an angle, ϕ, to the local electrode tangent, there will be a velocity component of $10000 \sin\phi$ m/s towards the cathode. For argon at the conditions believed to exist in the plasma ($T_e \sim 15000$ K, $T_i \sim$ 8000 K ahead of the shock, $\alpha \sim 0.6$), the ambipolar speed of sound is nearly 2500 m/s. If one

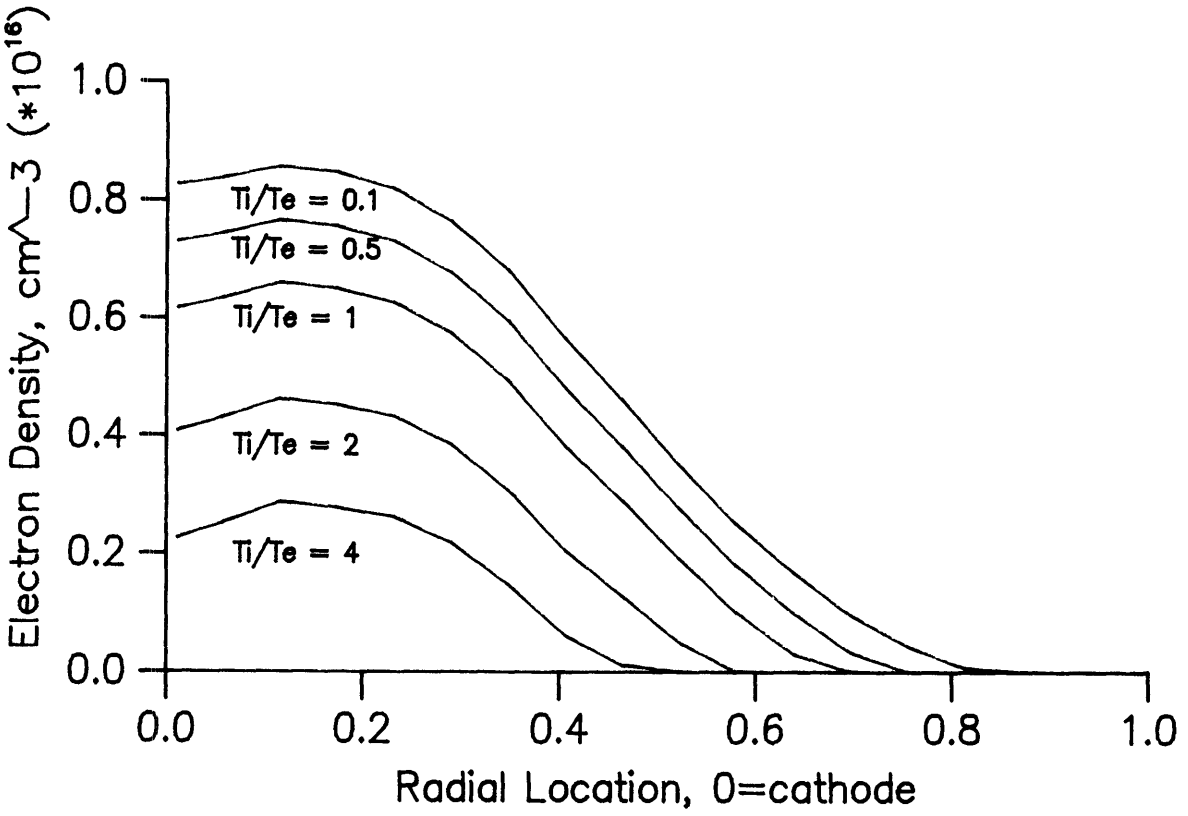

Figure 4.11. Radial profile of electron density in fully flared channel for various assumed values of T_i/T_e.

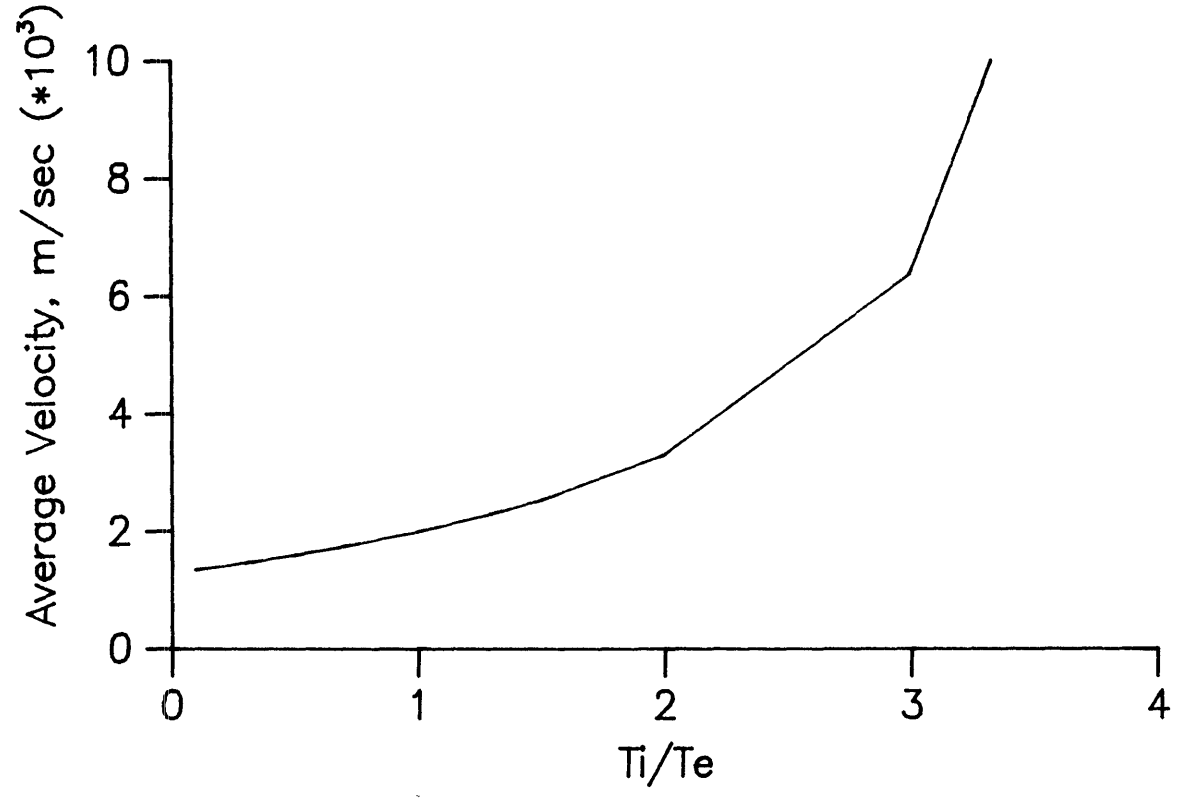

Figure 4.12. Average velocity of fully flared channel for various values of T_i/T_e.

assumes that the flow travels nearly perpendicular to the current lines (a weak assumption at best), then a current profile can yield a suitable estimate for ϕ. Probing of the channels has shown 45° to be a good approximation for ϕ. Thus, the flow has a Mach number of 2.86 towards the cathode. One would therefore expect a substantial shock to lie along the cathode. Using the relationship for temperature rise through a shock in a partially ionized plasma with T_e and α frozen, equation 4.5, an ion temperature increase by a factor of four within the shock layer could be expected.

$$4.5 \qquad \frac{T_{ia} + \alpha T_e}{T_{ib} + \alpha T_e} = \frac{(5M^2-1)\ (M^2+3)}{16M^2} \approx 3.42 \text{ for } M = 2.86 \text{ and } \gamma = 5/3$$

Where T_{ia} = ion temperature after shock
T_{ib} = ion temperature before shock
γ = ratio of specific heats
$M = \dfrac{u_{normal}}{\sqrt{\gamma R(T_{ib}+\alpha T_e)}}$

The final question to be answered is whether the shock layer can grow to occupy a substantial portion of the channel. To answer this, the simple model of flow over a hypersonic cone can be used. The actual situation depicted in figure 4.13a can be modeled by figure 4.13b. Hayes and Probstein[38] develop a relationship between cone angle, ϕ_c, and shock angle, ϕ_s.

$$4.6 \qquad \sin\phi_s = \sin\phi_c \,/\, \{(1-0.5\epsilon_f)\cos(\phi_s - \phi_c)\}$$

ϵ_f is the ratio of densities across the shock. For high mach numbers and $\gamma = 5/3$, ϵ takes on a limiting value of 1/4. For a cone angle of 45°, the shock angle is 55°. In the fully flared channel, the cathode is about 12 cm long and the shock layer thickness at the exit is about 2 cm. Thus, this model says that a shock layer would occupy most of the channel at the exit if it existed all along the cathode. In reality, the shock layer would stop perhaps at mid–channel after most of the flow had been turned inwards. This situation may be an explanation for the elevated ion temperature necessary for a plausible specific impulse. However, more work is needed to clarify the structure of the flow in this connection.

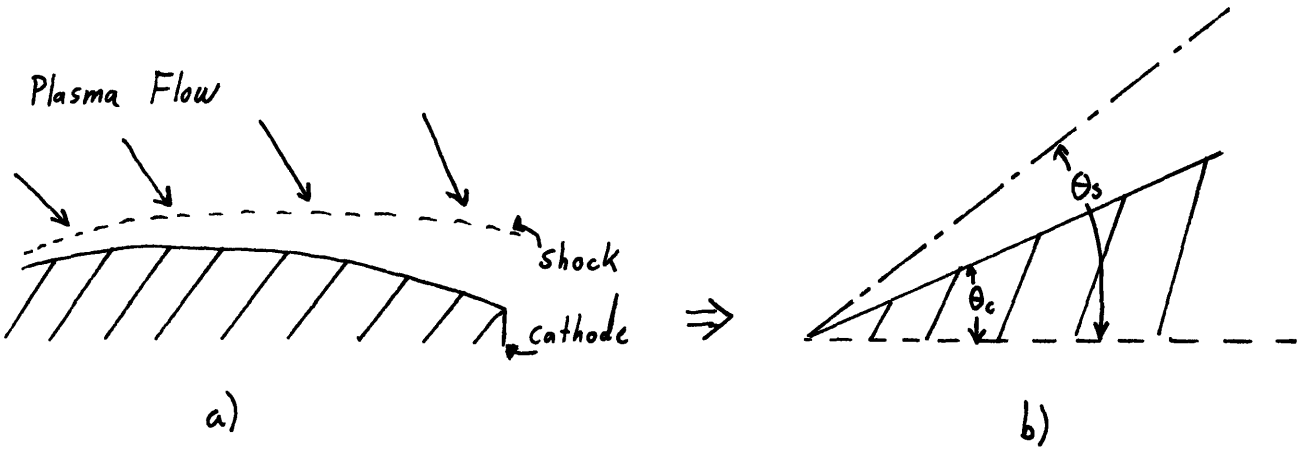

Figure 4.13. a) Schematic depiction of a cathode shock layer b) Illustration of geometry in simplified shock model.

A final attempt to measure density was made using the absolute line intensity method. The upper level density appearing in equation 2.11a was replaced with the total density according to the statistical mechanics relationship in equation 4.7.

$$\frac{n_i}{n_t} = \exp(-E_i/T) \,/\, Z(T) \tag{4.7}$$

Where n_i = density of ith level
E_i = excitation energy of ith level [eV]
$Z(T)$ = partition function

Of course, this is only valid if the equilibrium of the upper states extends down to the ground level. For a MPD plasma, one cannot expect this. In addition to this problem, the exponential term is extremely sensitive to fluctuations in temperature. For an argon line lying 21 eV above the ground level, a change in temperature from 1.2 eV to 1.5 eV would

imply a change in density of nearly two orders of magnitude! In short, this method was found to be unsuitable for total density calculations.

The absolute intensity measurement did have one use. The actual density of ions in certain excited states was calculated. The density suggested by the Hα profile was attributed to the ground state density (assuming $T_i/T_e = 1$). A Boltzmann plot was then made where the y–axis is the natural logarithm of the actual level densities. The result for the above onset, time integrated data in the fully flared channel is shown in figure 4.14. The ground level density appears to be above the value predicted by simply interpolating from the upper levels. This would be explained by radiative de–excitation where the middle energy levels, from 15 eV to 21 eV, are depopulated raising the ground level population above its expected value. The data is not conclusive enough to support this claim, however. These plots certainly raise confidence in the internal consistency of the density and temperature calculations for all the points very nearly lie on a line although two very different techniques were used to obtain them. Once again, the LTE assumption appears to valid throughout much of the levels.

The final result of this section concerns the effect of the startup transient on density measurements based on line intensities. Data was taken on the 4426.01 Å line of ArII above onset in the constant area channel. The data was temporally resolved in 100 microsecond increments over a 500 microsecond period. Figure 4.15 shows the results in arbitrary intensity units across the channel. The first 100 microseconds corresponds to the time necessary for the current and voltage to establish themselves at an equilibrium value. That interval is also over twice as bright as any subsequent interval. Any attempt to measure steady state densities based on line intensity must exclude this transient to get accurate results. As shown in the previous section, however, electron temperature based on relative line intensities was largely unaffected by the transient. A possible explanation of this initial intensity level can be found in the timing of the startup. The mass flow begins before current is supplied. Once the arc starts, the electrodynamic acceleration creates a high

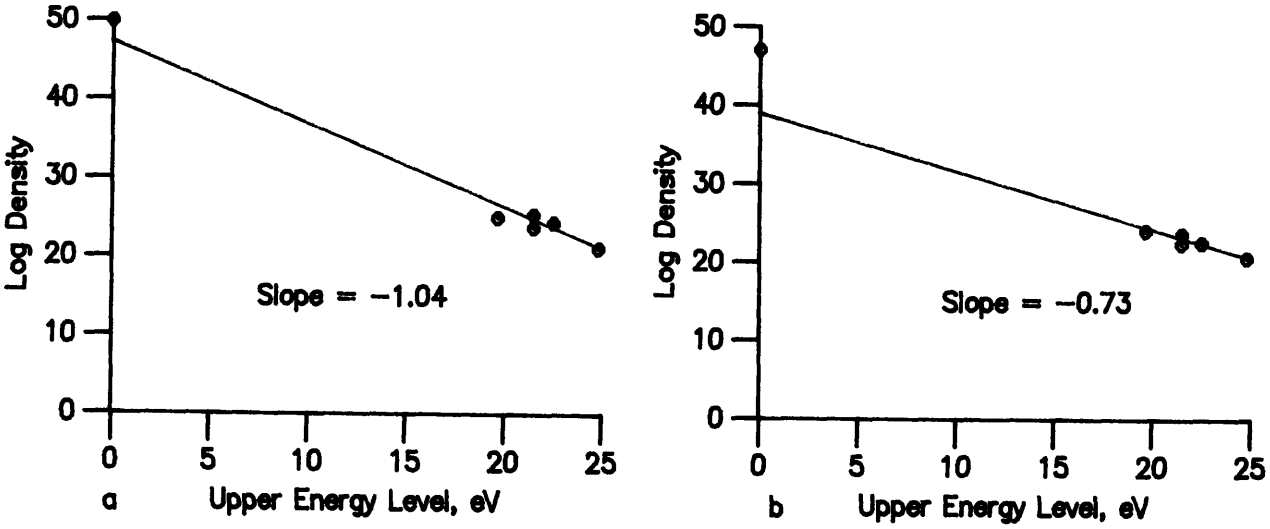

Figure 4.14. Sample Boltzmann plots from the fully flared channel including an estimate of the ground level density.

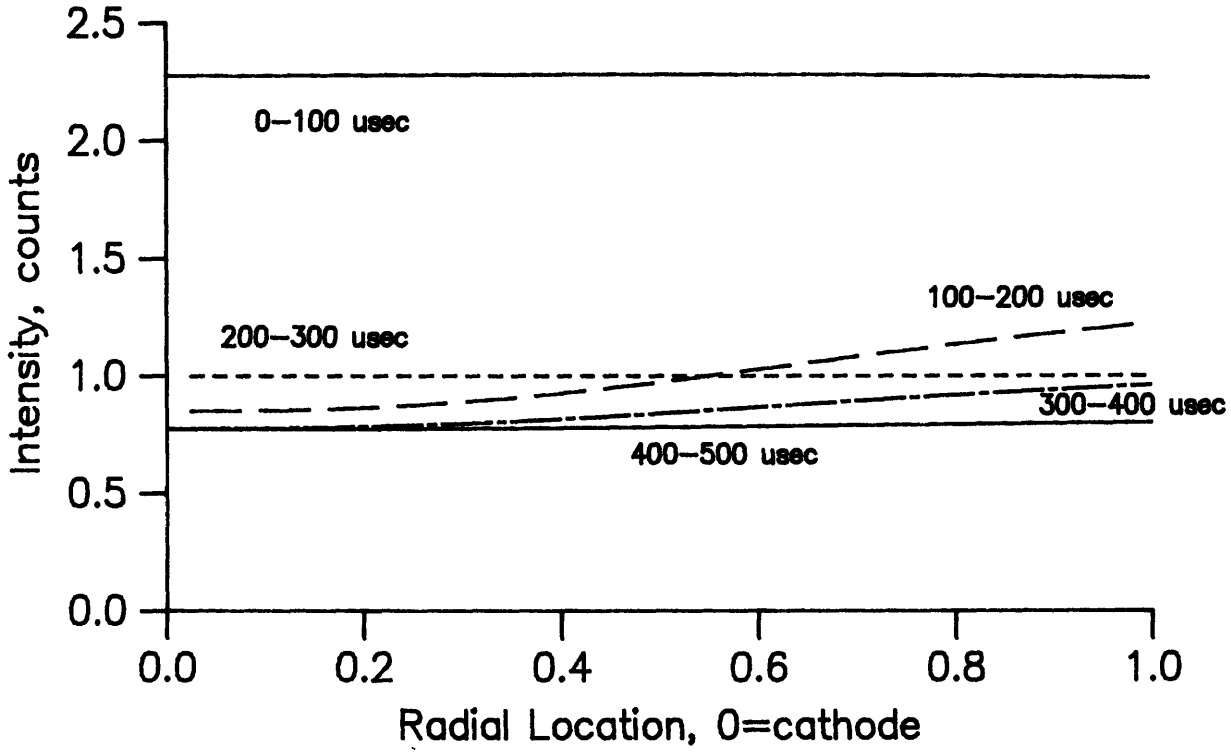

Figure 4.15. Time resolved radial intensity profiles of 4426.01 Å ArII line in constant area channel.

density wavefront that travels down the channel "pushing" the initial mass flow. The passage of this wavefront through the observation region accounts for the high initial intensity.

4.5 Ion Temperature Measurement

The ion temperature measurement was the most difficult and least successful measurement. Three attempts were made and each was thwarted by either the high ionization fraction or equipment limitations. It will be useful to review these attempts as there is no fundamental reason for their failure and future work may prove fruitful.

The first attempt was a straightforward recording of an argon Doppler broadening profile. The 4348.06 Å ArII line from the fully flared channel above onset was recorded in third order. The instrument bandwidth was about 0.1 Å and the total linewidth was only slightly higher. A maximum possible ion temperature of 15 eV at the cathode and 25 eV at the anode was the only possible conclusion of this data. By increasing the dispersion to the point where instrument bandwidth matches the theoretical third order resolving power of 0.02 Å, a reasonably accurate measure of ion temperature (± 1 eV) would be possible. Time constraints did not allow further attempts in this area.

The second attempt was to use the relative rotational transition line intensity method described in the chapter one. The plasma was seeded with nitrogen and the second positive nitrogen vibrational band was searched for but not found. The system calibration revealed a sharp response cutoff below 3700 Å. Evidently some element of the optical system was stopping the N_2 wavelengths. This technique still needs to be tested for MPD diagnostics however it is expected to be of use only for those areas where $T_i \lesssim 10000$ K, which, as discussed before, may exclude the cathode layer.

A third attempt was to record two hydrogen lines and use Fourier analysis to deconvolve the Stark and doppler broadening profiles as discussed in section II.4.3.

Unfortunately, the high ionization fraction of hydrogen permitted observation of only the Hα line. Perhaps the use of helium with its high ionization potential would permit application of this technique in future experiments. The flexibility of the data acquisition system allows any number of variations on this basic idea.

The analysis of the single Hα line in section 4.4 provided the only substantial information on ion temperature. As noted before in the discussion of figure 4.11, the ion temperature must be below about 1.0 eV near the anode to allow non–zero densities. Another interesting result is obtained by ascribing the entire Hα width to Doppler broadening. A maximum ion temperature can be calculated and is shown in figure 4.16. In the outer 35% of the channel, the ion temperature must be below 2 eV. Near the cathode, temperatures of 4 and 5 eV are entirely possible. This is therefore consistent with the observations made during the average velocity discussion.

While not definitive, these data are nevertheless interesting and give some indication of ion temperature within the MPD.

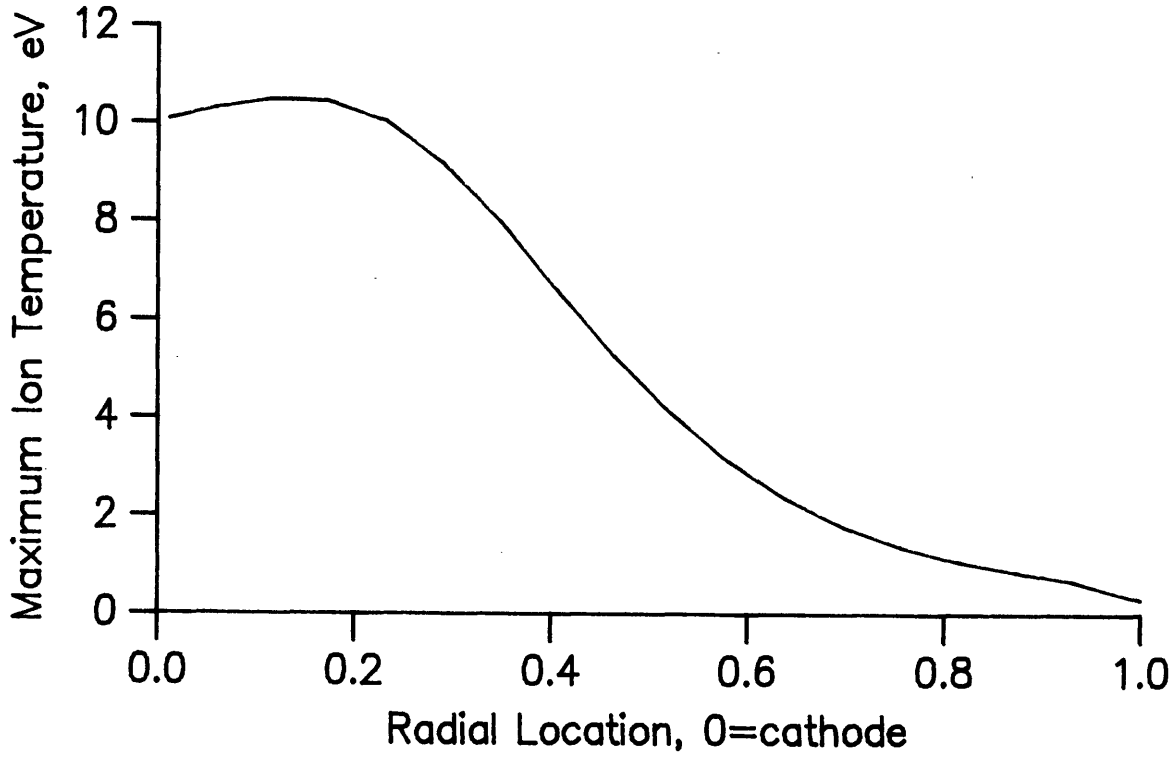

Figure 4.16. Maximum possible ion temperature in fully flared channel based on Hα profile.

Chapter 5

Conclusions and Recommendations

The purpose of this study was to develop a set of non–intrusive diagnostic techniques capable of rapidly and accurately characterizing a MPD plasma with both spatial and temporal resolution. A system based on an optical multichannel analyzer was selected and experimentally tested on several configurations of an axi–symmetric MPD arcjet. An analysis methodology was developed flexible enough to reduce all required data. The results were discussed in terms of model validities and possible plasma behavior.

The results showed that the data acquisition system was capable of measuring plasma densities and temperatures adequately. The system response was evaluated according to wavelength, intensity, and resolution in order to define the limits of its capability. The useful bandwidth is between 3700 Å and 9000 Å. The intensity response is linear with a dynamic range from 1 to 900 intensity units. A resolution of 0.1 Å was achieved.

The electron temperature was measured to an accuracy of about ±30% under a variety of conditions. Electrode flaring was found to reduce T_e by nearly a 40% when compared to the constant area case. One conclusion is that overall dissipation is reduced by electrode flaring. Inclusion of data from the transient start–up was not found to alter the measured distribution of temperature suggesting that temporal resolution is not necessary for a T_e measurement. Comparison of data from before and after initiation of voltage fluctuations shows a marked (~50%) reduction in T_e across the channel. Finally, the results showed agreement with the LTE assumption throughout energy levels that were measured.

Electron density in the fully flared channel was measured and found to range from 4×10^{15} cm^{-3} to 10×10^{15} cm^{-3} near the cathode to 0.1×10^{15} cm^{-3} to 1×10^{15} cm^{-3} near the anode. A substantial drop in density across the channel was observed and explained by the

presence of an anode starvation mechanism. Ionization of argon in the plasma was found to be nearly complete. In addition, the start–up transient was found to contribute a high fraction (~ 35%) of the total observed line intensity. Line intensity based measurements of density must therefore be temporally resolved.

Ion temperature measurements were largely unsuccessful. Detailed analysis of the Hα line yielded upper limits on the ion temperature ranging from 9 eV at the cathode to 0.5 eV at the anode. Consideration of specific impulse suggested ion temperatures three to four times greater than electron temperatures.

Recommendations for future work were clearly indicated by this first round of experimentation.

1. Develop a flat channel MPD to permit optical access to the arcjet interior and to eliminate the Abel inversion step in the analysis.

2. Seek out and encourage efforts to determine atomic transition probabilities for the higher lying lines used in electron temperature measurements. Specifically, obtain lower uncertainties to allow more accurate electron temperature calculations.

3. Investigate seeding with other Stark broadened atoms to overcome the density measurement limitations imposed by the high ionization fraction of hydrogen.

4. Install an additional optical system between the spectrometer and SIT camera to allow greater dispersion and, thus, wavelength resolution approaching 0.02 Å. This will permit Doppler broadened measurements to accurately determine ion temperature.

5. Extend the system's useful response to 3000 Å to permit further investigation of the rotational transition line intensity method for determining ion temperature.

In short, the diagnostic system developed here has met all initial requirements and shows considerable promise for future application.

LITERATURE CITED

[1] Martinez–Sanchez, M., and D. Heimerdinger, "Two–dimensional Analysis of an MPD Arcjet," AIAA Paper 85–2040.

[2] Martinez–Sanchez, M., "The Structure of Self–Field Accelerated Plasma Flows," AIAA Paper 86– .

[3] Kuriki, K., "Magnetoplasmadynamic Analysis of Plasma Acceleration," IEPC Paper 84–06.

[4] Kuriki, K., "MPD Arcjet Performance with Various Propellants," AIAA Paper 82–1885.

[5] King, D.Q., "Magnetoplasmadynamic Channel Flow Design of Coaxial MPD thrusters," PhD Thesis, Department of Mechanical and Aeronautical Engineering, Report No. 1544–T, Princeton University, Princeton, NJ, 1981.

[6] Griem, H.R., *Plasma Spectroscopy*, Mcgraw–Hill Book Co., New York, 1964, pp. 303–309.

[7] Griem, H.R., p. 303.

[8] Robinson, D., and P.D. Lenn, "Plasma Diagnostics by Spectroscopic Methods," Applied Optics, Vol. 6, No. 6, June 1967, pp. 983–1000.

[9] Griem, H.R., p. 299.

[10] Michels, C.J., and D.R. Sigman, "Exhaust Characteristics of a Megawatt Nitrogen MPD–Arc Thruster," AIAA Journal, Vol. 9, No. 6, June 1971, pp. 1144–1147.

[11] Michels, C.J., J.R. Rose, and D.R. Sigman, "Electron Number Density and Temperature in MPD–Arc Thruster Exhausts," AIAA Journal, Vol. 10, No. 11, Nov. 1972, pp. 1395–1396.

[12] Griem, H.R., p. 307.

[13] Burgess, D.D., and J. Cooper, "A new method of measuring electron temperatures in plasmas in the absence of local thermodynamic equilibrium," Proc. Phys. Soc., Vol. 86, 1965, pp. 1333–1341.

[14] Burgess, D.D., and J. Cooper, "An interferometer designed for the detection of small shifts in wavelength of spectral lines emitted by plasmas, and for measuring the ratio of such shifts to the line width," J. Sci. Instrum., Vol. 42, 1965, pp. 829–833.

[15] Robinson, D., and R.W. Nicholls, J. of Quant. Spect. Radiative Transfer, Vol. 1, No. 76, 1961.

[16] *Plasma Diagnostics*, ed. by W. Lochte–Hotgreven, North Holland Publishing Co., Amsterdam, 1968, p. 184.

[17] Cremers, C.J., and R.C. Birkebak, "Application of the Abel Integral Equation to Spectrographic Data," Applied Optics, Vol. 5, June 1966, pp. 1057–1064.

[18] Berge and Richter, AFSC Report 61 (052)–797, 1966.

[19] Keefer, D.R., L. Smith, and S.J. Sudharsanan, "Abel Inversion using Transform Techniques," University of Tennessee Space Institute, Tullahoma, Tennessee, 1986.

[20] Bracewell, R.N., *The Fourier Transform and Its Applications*, McGraw–Hill Book Co., New York, 1965.

[21] Candel, S.M., "An Algorithm for the Fourier–Bessel Transform," Computer Physics Communications, Vol. 23, 1981, pp. 343–353.

[22] Smith, M.L., "Nonstationary Noise Effects in the Abel Inversion," University of Tennessee Space Institute, Tullahoma, Tennessee.

[23] Robinson, D., and P.D. Lenn, "Plasma Diagnostics by Spectroscopic Methods," Applied Optics, Vol. 6, No. 6, June 1967, pp. 983–1000.

[24] Benjamin, J.R., and C.A. Cornell, *Probability, Statistics, and Decision for Civil Engineers*, McGraw–Hill Book Co., New York, 1970, p. 433.

[25] Griem, H.R., p. 145.

[26] Mitchner, M., and C.H. Kruger, *Partially Ionized Gases*, John Wiley and Sons, New York, 1973.

[27] Wilson, R., "The Spectroscopy of Non–Thermal Plasmas," J. Quant. Spect. Radiative Transfer, Vol. 2, pp. 477–490.

[28] *Plasma Diagnostic Techniques*, ed. by R.H. Huddlestone and S.L. Leonard, Academic Press, New York, 1965, p. 269.

[29] Lorentz, H.A., Proceedings of the Academy of Science, Amsterdam, Vol. 8, 1906, p. 591.

[30] Kolb, A.C., and H.R. Griem, Phys. Rev., Vol. 111, 1958, p. 514.

[31] *Plasma Diagnostic Techniques*, p. 270.

[32] *Plasma Diagnostic Techniques*, p. 269.

[33] Bittencourt, J.A., *Fundamentals of Plasma Physics*, Pergamon Press, Oxford, 1986, p. 192.

[34] Hill, R.A., "Tables of Electron Density as a function of the halfwidth of Stark–Broadened Hydrogen lines," J. Quant. Spect. Radiative Transfer, Vol. 4., 1964, pp. 857–861.

[35] *Plasma Diagnostic Techniques*, p. 303.

[36] Rudolph, L.K., R.G. Jahn, K.E. Clark, and W.F. von Vaskowsky, " Onset Phenomena in Self–Field MPD Arcjets," AIAA Paper 78–653.

[37] Heimerdinger, D.,"Fluid Mechanics in a Magnetoplasmadynamic Thruster," PhD Thesis, Department of Aeronautics and Astronautics, Massachusetts Institute of Technology, Cambridge, MA, 1988.

[38] Hayes, W.D., and R.F. Probstein, *Hypersonic Flow Theory*, Academic Press, New York, 1964.

[39] Griem, H.R., p. 146.

[40] Griem, H.R., p. 144.

[41] Bittencourt, J.A., *Fundamentals of Plasma Physics*, Pergamon Press, Oxford, 1986.

[42] Van Driest, NACA Technical Note 2597, 1952.

[43] Mitchner, M., and C.H. Kruger, p. 271.

[44] Wiese, W.L., et al., "Atomic Transition Probabilities Sodium through Calcium: A Critical Data Compilation," National Bureau of Standards, AD–696–884, Washington D.C., 1969.

Appendix 1

LTE Validity Model Derivation

A number of simple models were used to describe the various rate processes relevant to local thermodynamic equilibrium (LTE).

1. Radiative transition rate, $R_{nn'}$:

This model follows the one given by Griem[39]. The total radiative rate out of a level n to a lower lying level n' is:

A1.1 $$R = \sum_{n'<n} A_{nn'} \quad \text{where } A_{nn'} = \text{transition probability for level n to } n'$$

For a hydrogenic system, this summation can be approximated by:

A1.2 $$R_n = \sum_{n'<n} A_{nn'} \approx \frac{c r_0^2 z^4}{a_0^3 n^{4.5}}$$

Where
- c = speed of light in vacuum
- r_0 = classical electron radius
- z = number of effective charges
- a_0 = Bohr radius
- n = principal quantum number

Thus,

A1.3 $$R_n \approx 1.6\text{x}10^{10} \frac{z^4}{n^{4.5}} [\text{sec}^{-1}]$$

2. Collisional transition rate, $C_{n'n}$:

Generally speaking, any collisional rate can be expressed as:

A1.4 $$C_{n'n} = \langle \sigma_{n'n} v \rangle_{avg} n_e$$

Where
- $\sigma_{n'n}$ = cross section for collision
- v = relative velocity

Assuming a Maxwellian electron distribution and a hydrogenic system, this rate can be rewritten as[40]:

A1.5 $$C_n = \frac{9\text{x}10^{-8}}{4\ z^3} n_e n^4 \left\{ \frac{z^2 E_h}{T} \right\} [\text{sec}-1]$$

Where
- E_h = ionization potential of hydrogen
- n_e = electron density [cm^{-3}]

In this expression, an exponential term has been replaced by unity.

3. Ambipolar diffusion rate, D:

This discussion relies on reference 41. The rate of recombination due to diffusion is:

A1.6 $$\dot{n}_{e_{diff}} = \nabla\cdot(n_e D_a \frac{\nabla p}{p}) = D_a \nabla^2 n_e$$

Where D_a = ambipolar diffusion constant

The assumption that $T_e = T_i$ was also used. If one assumes a parabolic distribution for n_e with $\bar{n}_{eo}$ being the centerline density, and the definition of the diffusion coefficient is used:

A1.7 $$D_a \equiv \frac{2kT_e}{m_{in}\nu_{in}}$$

Where m_{in} = reduced mass of ions and neutrals
ν_{in} = collision frequency of ions and neutrals

The following relation for the rate of depopulation is arrived at:

A1.8 $$D = \frac{1.31x10^{15}\sqrt{T_e}}{R^2 \frac{1-\alpha}{\alpha} n_e}$$

Where R = half characteristic length of diffusion [m]
α = ionization fraction

The parabolic distribution assumption is akin to an assumption of fully developed flow. This can be simply validated by an application of a flat plate compressible boundary layer model that includes heat conduction. Reference 42 gives the results for such a model.

A1.9 $$\frac{\delta}{x}\sqrt{R_{ex}} \simeq 6$$

Where δ = boundary layer thickness
R_{ex} = Reynolds number based on x

The Reynolds number can be estimated as follows (for the conditions estimated in this diagnostic):

μ_∞= 3.2x10 for $\alpha = 0.9$ $\qquad \rho_\infty u_\infty = \dot{m}/A$

x = plate length $\qquad R_{ex} = \frac{\rho_\infty u_\infty x}{\mu_\infty} \simeq 1200$

This gives a boundary layer thickness of 0.02 meter which is half of the channel height. Therefore, one may rightly assume fully developed flow and the parabolic distribution model is appropriate.

4. Three–body recombination rate, R:

A number of detailed calculations exist for this rate. One given by Gurevich and Pitaenskii[43] will be used.

A1.10 $$\dot{n}_{e_{recomb}} = -1.11\text{x}10^{-26}\, n_e^3\, T^{-4.5} \ln\Lambda \quad \text{where } \Lambda = \text{log factor of T}$$

The rate per ion can be estimated by $\dot{n}_e/n_e$:

A1.11 $$R \cong 1.11\text{x}10^{-26}\, n_e^2\, T^{-4.5} \ln\Lambda$$

As always, the units on electron density are cm^{-3}.

5. Advection rate, A:

The advection rate can be approximated by:

A1.12 $$A = \frac{1}{n_e}\frac{dn_e}{dt} = \frac{1}{n_e}\frac{dn_e}{dx}\frac{dx}{dt} \approx \frac{1}{n_e}\frac{n_e}{R}V = \frac{V}{R}$$

Where V = characteristic velocity
R = characteristic length

This nonequilibrium process will only be significant if there is a substantial temperature gradient in the flow direction. Otherwise, the introduction of upstream ions will not upset the local equilibrium. That is to say, if everything is the same in the flow direction then convection does not really matter.

Appendix 2

Interface Circuitry

To allow proper data transfer between the IBM 9000 computer and the Model 1216 detector controller, an interface circuit was necessary to match the "handshake' conventions. Figure A2.1 gives a schematic for this circuit.

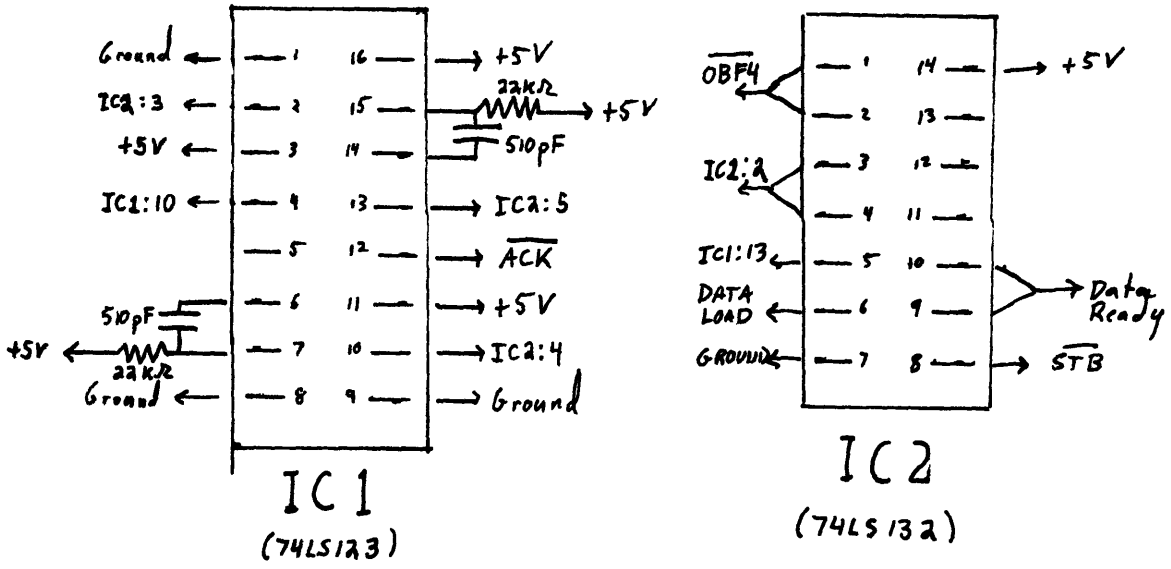

• Data leads connected as per equipment instructions

Figure A2.1. Circuit schematic of interface between Model 1216 controller and IBM System 9000 computer.

Appendix 3

Design for Improved Exit Optics

A simple optical system between the spectrometer exit plane and the SIT camera face will enable adjustment of wavelength dispersion. With the SIT camera mounted flush to the spectrometer, the dispersion is fixed at 0.16 Å/pixel in first order. With an adjustable dispersion, the resolution could be brought down to match that of the spectrometer.

Schematically, the system is composed of two components: a mounting rail and a cylindrical lens with a vertical axis (see figure A3.1). The lens images the spectrometer focal plane on the SIT target face. The spacing and lens' position on the rail is dictated by the lens focal length, f, and desired magnification of the dispersion, D, through the classical lens maker formula and trigonometry.

A3.1 $$\frac{1}{f} = \frac{1}{d_1} + \frac{1}{d_2}$$

A3.2 $$\frac{D_2}{D_1} = \text{magnification} = \frac{d_2}{d_1}$$

Thus, the design must permit d_2 and d_1 to be independently adjusted. The use of a cylindrical lens preserves the spatial resolution or spectral line "height". One possible trouble arises when one recalls that the exit plane contains an image, not a source. Each point "emits" light in a cone in a certain direction. The cone size in steradians is specified by the spectrometer focal length and the direction is specified by the point's location in the exit plane. It is conceivable that light near the edge of the plane may not be completely collected by the lens and artificial intensity variations may be introduced. One can model this simply. Such a calculation has been done and has shown that for typical lens (diameter ~ 2 inches, focal length ~50 cm) light will be uniformly collected from a region at least one centimeter wide, which is all that is necessary. Furthermore, one can use a larger lens to extend the constant light collection region or even just calibrate the effect out of the data.

Mechanically speaking, the system would be composed of four elements. First, a

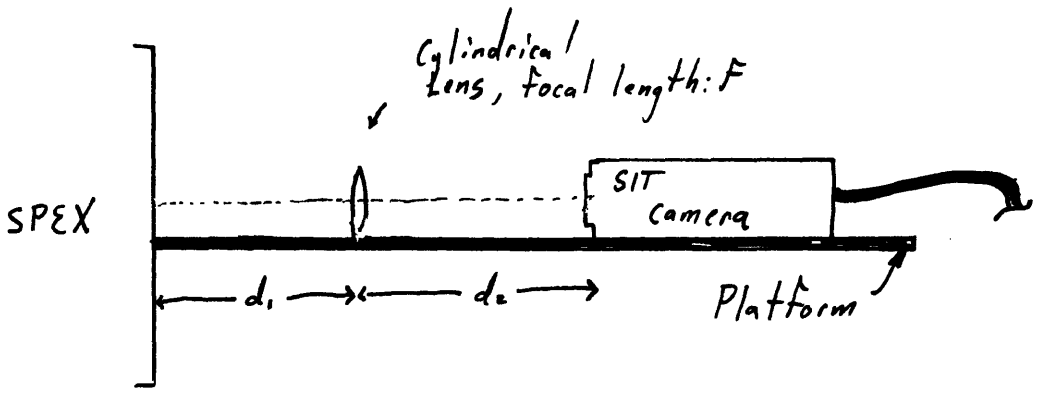

Figure A3.1. Schematic showing an improved spectrometer exit optical arrangement.

platform must be made to mount on the spectrometer. It must be rigid enough to withstand the large bending moment generated by the SIT camera. Also, a standard optical rail should be mounted on its top surface. Figure A3.2 gives an example. Secondly, a cradle adapter must be made to mount the SIT camera on the optical rail. The design must be such that the SIT camera position can be easily adjusted. Thirdly, a cylindrical lens with a standard mount must be acquired. Finally, the whole system must be shrouded in a light shield to exclude stray light.

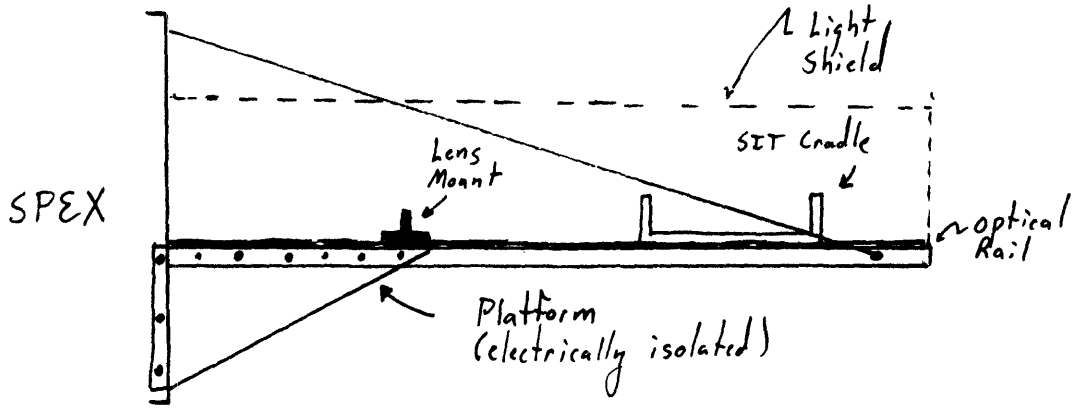

Figure A3.2. Sketch of a possible platform arrangement for improved optical system.

Appendix 4

Tabulation of Atomic Constants

Three quantities were necessary to convert measured intensities to actual populations. These quantities were:

1. g : Degeneracy of the lower level of the transition.

2. λ : The wavelength of the transition.

3. f : The absorption oscillator strength which is related to the atomic transition probability.

g and λ are generally known to an extremely high accuracy and, hence, no uncertainty was used for them. The oscillator strength, however, singlehandedly introduced the most uncertainty into the electron temperature measurement. Table A4.1 lists the values used for each of the spectral lines used in this study[44]. The letter next to the oscillator strength is a code for the uncertainty associated with it: A = < 25% B = < 50%.

TABEL A4.1 ATOMIC CONSTANTS

λ, Å	E_{upper}, eV	g_{lower}	f
3729.60	24.8	10	0.67 B
3737.90	24.8	6	0.64 B
4042.90	21.5	4	0.34 B
4072.01	21.5	6	0.142 A
4079.60	21.5	4	0.043 B
4103.91	22.7	6	0.22 B
4156.09	22.6	4	0.10 B
4226.99	24.3	4	0.16 B
4448.88	24.3	6	0.19 B
4609.60	21.1	6	0.387 A